

AFTT/GSO/ENG/93D-1

AD-A274 040



①

S DTIC
ELECTE
DEC 23 1993
A

DESIGN ANALYSIS OF A COMBINED
OPTICAL/LADAR DEEP-SPACE
SURVEILLANCE SATELLITE

THESIS

Bradley K. Fournier
Captain, CAF

AFTT/GSO/ENG/93D-1

Approved for public release; distribution unlimited

93 12 22 1 0 6

93-30993



95 pgs

DESIGN ANALYSIS OF A COMBINED OPTICAL/LADAR DEEP-SPACE
SURVEILLANCE SATELLITE

THESIS

Presented to the Faculty of the Graduate School of Engineering

of the Air Force Institute of Technology

Air University

In Partial Fulfillment of the

Requirements for the Degree of

Master of Science in Space Operations

Bradley K. Fournier, B. Sc.

Captain, CAF

NOVEMBER, 1993

Accession For	
NTIS CRA&I	<input checked="checked" type="checkbox"/>
DTIC TAB	<input type="checkbox"/>
Unannounced	<input type="checkbox"/>
Justification	
By	
Distribution /	
Availability Codes	
Dist	Avail and/or Special
A-1	

DTIC QUALITY INSPECTED 3

Approved for public release; distribution unlimited

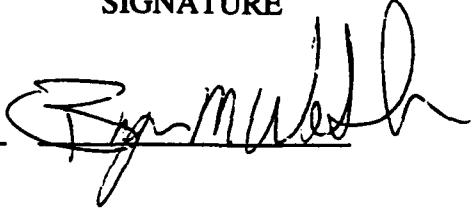


THESIS APPROVAL

STUDENT: Bradley K. Fournier

CLASS: GSO 93D

THESIS TITLE: DESIGN ANALYSIS OF A COMBINED OPTICAL/LADAR
DEEP-SPACE SURVEILLANCE SATELLITE

DEFENSE DATE: 17 Nov 93

COMMITTEE:	NAME/DEPARTMENT	SIGNATURE
Advisor	<u>Byron M. Welsh / ENG</u>	
Reader	<u>Michael C. Roggemann / ENP</u>	
ENS Representative/Reader	<u>Thomas S. Kelso / ENS</u>	

Preface

The purpose of this research was to determine the performance requirements of a combined optical/LADAR space-based system in order to detect and track deep-space satellites from a near-earth orbit satellite. The research examines the current feasible laser transmitters and associated optics and detectors. The results show that detection and tracking of deep-space satellites from a low-earth orbit using LADAR is possible but the range resolution accuracy depends on the time between false alarms and target size. The capability to track deep-space satellites using detectors operating in visible wavelengths from low-earth orbits can meet or exceed that currently provided by GEODSS.

In accomplishing this research I had a help and support from many sources. I wish to thank my thesis advisor, Dr. Byron Welsh, for providing me with exceptional guidance and putting up with my continuous interruptions of his busy schedule. I also wish to thank my readers, Lt Col Thomas Kelso and Dr. Mike Roggemann, for providing valid comments and input into a seemingly overwhelming task. Finally, and most important of all, I wish to thank my wife, Therese, and daughters, Jacqueline and Michelle. Their patience and encouragement is the sole reason I survived to see this project completed.

TABLE OF CONTENTS

	Page
Preface	ii
List of Figures.....	vi
List of Tables	viii
I. Introduction	1-1
Background.....	1-1
GEODSS Limitations	1-2
Research Objective	1-3
Scope and Limitations	1-3
Methodology	1-4
II. Literature Review.....	2-1
Introduction	2-1
GEODSS	2-1
Ground-Based Laser Radar	2-4
Space-Based Visible Sensor	2-6
Space-Based Multi-Spectral Sensor	2-7
III. Optical Detection	3-1
Introduction	3-1
Signal-to-Noise Ratio	3-2
Shot Noise (Photon Noise).....	3-3
Thermal Noise (Johnson Noise or Nyquist Noise).....	3-4
Background Noise	3-5
Dark Noise	3-5
Local Oscillator Noise	3-6
Detection Techniques.....	3-6
Coherent Detection.....	3-7

Incoherent Detection (Direct Detection or Energy Detection).....	3-11
Comparison of SNRs of Coherent and Incoherent Systems	3-15
SNR of Coherent Systems.....	3-15
SNR of Incoherent Systems	3-16
Pulse Integration	3-19
LADAR Range Equation.....	3-21
System Efficiency	3-23
Optical Transmission	3-23
Transmitter Efficiency	3-23
Receiver Efficiency	3-25
IV. System Components and Design.....	4-1
Introduction	4-1
Laser Transmitters	4-1
Carbon Dioxide Laser.	4-2
Nd:YAG Laser	4-2
InGaAs laser	4-2
GaAlAs Lasers.....	4-3
Optics	4-4
Visible Detector	4-7
LADAR Detector	4-9
Satellite Orbit.....	4-10
V. Design Selection and Performance Analysis	5-1
Introduction	5-1
Transmitter Selection	5-1
CO2 Laser Transmitter.....	5-5
Nd:YAG Laser transmitter.....	5-6
InGaAs Laser Transmitter.....	5-7
GaAlAs Laser Transmitter	5-7
Alternate Laser Transmitter	5-7
Detection Capabilities of Proposed and GEODSS Systems	5-15
Proposed System Detection Capabilities	5-16
GEODSS Detection Capabilities.....	5-16
VI. Conclusions and Recommendations	6-1
Conclusions	6-1

Recommendations for Further Study	6-4
--	------------

List of Figures

Figure	Page
2.1 Wavelength dependencies of the quantum efficiencies of a typical S-20 photocathode	2-3
2.2 Quantum efficiency of back-illuminated imager	2-8
3.1 Detection Statistics - Incoherent Detection of Nonresolved Tough Target	3-14
3.2 Comparative performances of heterodyne and energy detection - nonresolved target.....	3-18
3.3 Integration efficiency as a function of number of pulses integrated.....	3-20
3.4 Far field on-axis efficiency as a function of obscuration ratio and aperture to beamwidth ratio	3-24
3.5 Transmitter efficiency as a function of off-axis parameter X	3-25
3.6 Direct detection efficiency as a function of obscuration ratio and d	3-27
3.7 Airy spot radius and F-number as a function of obscuration ratio.....	3-28
3.8 Receiver efficiency for uniform local oscillator as a function of the obscuration ratio and the ratio of the detector radius to the Airy spot size (r).....	3-29
3.9 Receiver efficiency for Gaussian local oscillator as a function of obscuration ratio and the ratio of the detector radius to the Airy spot radius	3-30
4.1 Schematic of Roving Fovea	4-5
4.2 PDOP 4 altitude as a function of time for 0° N	4-12
4.3 PDOP 4 altitude as a function of time for 30° N	4-12
4.4 PDOP 4 altitude as a function of time for 60° N	4-13
5.1 Required SNR as a function of probability of false alarm	5-11
5.2 Detection range as a function of range resolution for Nd:YAG	5-13
5.3 Detection range as a function of range resolution for GaAlAs	5-14

5.4 Range resolution as a function of target area for GaAIAs	5-15
5.5 Proposed sensor and GEODSS SNRs as a function of target area	5-18
5.6 Probability of false alarm as a function of time between false alarms.	5-18
5.7 Required signal-to-noise ratio as a function of probability of false alarm.	5-19

List of Tables

Table	Page
4.1 Maximum Usable Optics Diameter for Various Wavelengths as a Function of Achievable Beam Jitter	4-6
4.2 Angular Resolution and Sensor Field-of-View for Various Entrance Pupil Diameters.....	4-7
5.1 Peak Power for Selected Transmitters.....	5-2
5.2 Detection Efficiency Parameters for Selected Transmitters.....	5-3
5.3 Detection Efficiencies for Selected Transmitters	5-4
5.4 Received Power for Selected Transmitters	5-4
5.5 Received Signal-to-Noise Ratios.....	5-7
5.6 CCD Detector Signal-to-Noise Ratios	5-9

Abstract

This research determines the performance requirements of a combined optical/LADAR space-based system in order to detect and track deep-space satellites from a near-earth orbit satellite. The research derives the necessary equations to compare both direct and heterodyne detection techniques. The selection of the candidate laser systems is based on current space-developed LADAR technology. The selection of the detector, detector size, and optic size are determined in order to maximize the signal-to-noise ratio. The analysis includes the effects of beam truncation, obscuration, pixel geometry, and background radiance. A target in geosynchronous orbit is used to determine minimum detection capability.

The results indicate that the direct detection technique with a GaAlAs semiconductor laser and a charge-couple device detector provided the best signal-to-noise ratio for the range selected. The thesis shows the dependence of the range resolution on target detection range as well as target size. In addition, the visible detection capability of the smallest entrance pupil system is compared with that of GEODSS. For the parameters chosen, the results indicate that this system should, on average, be able to detect objects of smaller size than GEODSS.

DESIGN ANALYSIS OF A COMBINED OPTICAL/LADAR DEEP-SPACE SURVEILLANCE SATELLITE

I. Introduction

Background

The mission of space surveillance started with the launch of Sputnik I in October 1957. Although President Eisenhower and his senior advisors knew that the Soviet Union was close to having the capability to launch artificial satellites, the American public were shocked (38:39). This resulted in a public outcry for increased expenditure on missile and space programs. One of the space programs of interest was that of space surveillance. Scientists and engineers at Hanscom Field, Massachusetts, were asked to devise methods to observe Soviet satellites and calculate their orbits (13:585).

This concern for surveillance provided a catalyst for the evolution of a Space Surveillance Network (SSN). The network is a conglomeration of optical and radar sensors used in support of the space surveillance mission to detect, track, identify and catalog all objects in earth orbit (2:12-10). The data from these sensors is forwarded to the United States Space Command (USSPACECOM) Space Surveillance Center (SSC) inside Cheyenne Mountain. The SSC uses the data from these objects to create orbital element (OE) sets which allow them to predict the position of any object at any time. These predictions are then used to provide collision avoidance, satellite decay and impact predictions, satellite maneuver identification, warning of a satellite passing over a specific geographic area, and warning of attack on US space assets (2:12-10). In order to provide the most accurate position predictions possible, it is essential that the orbital element sets be accurate and timely.

In order for the SSN to continuously track the approximately 6,000 man-made objects in earth orbit, the space environment is divided into two regions: near-earth and deep-space. An orbital period of 225 minutes is the dividing line for the two regions which corresponds to a circular orbit altitude of slightly less than 6,000 kilometers. While there are some active ground-based sensors capable of detection of deep-space satellites, the primary system in use is the Ground-Based Electro-Optical Deep-Space Surveillance System (GEODSS).

GEODSS Limitations

GEODSS is a passive optical system that operates in the visible spectrum. Since GEODSS relies on reflected sunlight for satellite detection, its operation is restricted to night-time, clear-weather conditions. Bright sky conditions, such as twilight, or the 7-day period centered on the full moon, seriously affect GEODSS capability. In addition, when there is less than 1 percent of clear night sky, tracking is not even attempted. This weather condition often exists for 30 percent to 60 percent of the available tracking time (22:5). Combining this with the average expected hours of darkness per night and the probability of clear skies, the average 24-hour availability of GEODSS is 14 percent (8:9).

This limitation in the operational capability of GEODSS has contributed to the widening gap between the estimated population of deep-space objects, and the SSN-monitored population (8:1). This problem will be compounded by the expected increase in objects in deep-space orbits. As of 11 Nov 1992, there were 1,257 deep-space objects in the space catalog and this number is expected to increase to nearly 2,000 by the year 2002 (39). The only current upgrade planned for GEODSS is the replacement of the SIT Vidicon detectors with charge-coupled devices (CCDs). While this may increase their detection capability, it will not have a large impact on their availability. To meet future

requirements for deep-space surveillance requires either more GEODSS sites or a new surveillance system

In order to provide global coverage, the GEODSS sites are approximately equally spaced as close to the equator as possible. This requires that US facilities be maintained in foreign countries. With increased pressure to reduce the number of foreign facilities, a proposed increase in the number of deep-space ground sites will likely meet with some opposition. In addition, access to these facilities may become a problem if political issues arise between the US and the host country. This problem can be alleviated by placing the sensors on satellites and accomplishing the task of space surveillance from space.

Research Objective

The objective of this research is to analyze the expected performance of a combined optical/LADAR deep-space surveillance satellite. This performance is then compared with that of the current GEODSS system to determine its advantages and limitations.

Scope and Limitations

The analysis is based on determining the system performance required in order to achieve detection and tracking of deep-space satellites. Successful detection will be assumed if the required signal-to-noise ratio (SNR) is achieved. In order to determine the SNR, the research will examine the current methods of optical detection as well as the characteristics of the optics, laser, detector, and background radiance. System components will be selected from available technology. The performance of this system will be compared to that of GEODSS.

This research is limited to a performance analysis of selected technologies. No cost analysis or detailed satellite design are performed.

Methodology

The research is broken into three major areas: (1) optical detection, (2) system components and design, and (3) design selection and performance analysis. These three major areas will be discussed in Chapters 3-5 which follow the literature review in Chapter 2. Chapter 6 will conclude the research and provide a summary of the results.

II. Literature Review

Introduction

This chapter reviews the literature pertinent to this thesis. The review includes a description of the current GEODSS system as well as several proposed systems to replace GEODSS. These proposed systems to be examined are a ground-based LADAR sensor, a space-based visible sensor, and a space-based multi-spectral sensor.

GEODSS

The GEODSS system was designed as a replacement for the Baker-Nunn camera system. Installed in the early 1980s, the GEODSS system provided greater tracking capacity, quicker response to orbital maneuvers, and ability to detect beyond the 14th magnitude limitation of the Baker-Nunn system (4:469). In order to provide global coverage, original plans called for five GEODSS sites to be relatively evenly spaced as close to the equator as possible. Only four of the five sites were constructed and with the recent closure of the site located at Taegu, Korea, only three of the original sites are still operative. The sites are located at Socorro, NM; Maui, HI; and Diego Garcia in the Indian Ocean (1:59). In addition to these sites, there is a transportable-optical system in place at San Vito, Italy. Although the system is slightly different than the GEODSS sites, its capability for detection of deep-space objects is comparable (26). Therefore, for the purposes of this study, the GEODSS system will be considered to consist of these four GEODSS sites.

Each GEODSS site is equipped with two main 40-inch (1-meter) telescopes and one 15-inch auxiliary telescope. The two main telescopes each weigh approximately 3,200 pounds and use a Ritchey-Cretien design for the folded optics to achieve an 86-inch focal length. Line-of-sight light entering the telescope's aperture is reflected off a

hyperbolic mirror to a secondary mirror, which in turn reflects the light to a group of refracting lenses. The obscuration by the secondary mirror decreases the clear aperture area from 0.785 m^2 to 0.46 m^2 (22:58). Each of the main telescopes has a 2.1° field-of-view and is housed in a 20-foot diameter tower whose mount system provides a maximum slew rate of 2 degrees per second and a positional accuracy of 1.5 arc seconds (31:47). This provides a maximum scan rate of 2,400 square degrees per hour. The auxiliary telescope utilizes a folded-Schmidt design with a clear aperture of 15 inches, a focal length of 30 inches, a 6-degree field-of-view, and an obscuration ratio of 0.643. Its main purpose is to track fast-moving satellites in near-earth orbits. The auxiliary telescope has a 1.5 arc second positional accuracy and a slew rate of 15 degrees per second resulting in a maximum rate of 15,000 square degrees per hour (8:8).

The key element in the design of the GEODSS system is a device called the silicon intensified target (SIT) vidicon tube. This device is installed at the focal plane of the field group lenses in the camera. At the front of this device is a photocathode which emits electrons when struck by the photons of light energy entering the system. These electrons are then focused onto an 832×832 array of silicon elements which create electron-hole pair charge carriers when struck by the electrons. Normally the image only occupies 625 of the 832 elements. By scanning this array with an electron beam, a video image of the incident light is created (6:4-9). Using this device GEODSS has the capability to track and record objects down to the 17th magnitude. When atmospheric conditions are excellent, objects down to the 19th magnitude are visible (4:340).

The GEODSS system is unfiltered and operates in the 0.3 to 0.86 wavelength band. This band is determined from the responsivity of the S-20 photocathode. A graph of the photocathode efficiency versus wavelength is depicted in Figure (2-1) (41:5). The average efficiency of the 80 mm diameter photocathode is approximately 7 percent. The gain provided by accelerating the photoelectrons onto the 32-mm silicon array is

approximately 2000. It is this high pre-scan gain that attempts to make the GEODSS system being photon noise limited by overcoming the typical dark current of 1×10^{-8} A (22:53).

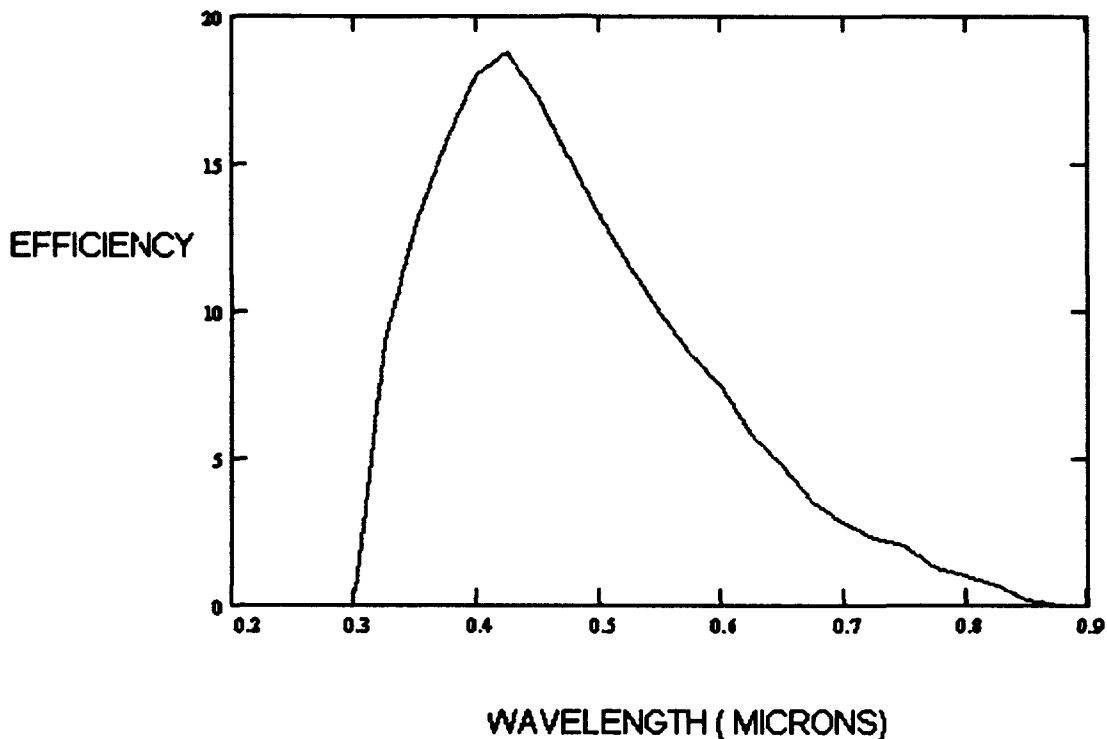


Figure 2.1 Wavelength dependencies of the quantum efficiencies of a typical S-20 photocathode

In operation, the system must compensate for the rotation of the earth in order to provide a still image. To accomplish this the system uses a sidereal drive mechanism which moves the telescope opposite and equal to the earth's rotation, causing the stars to appear inertially fixed while the satellites appear as streaks of light. Once the telescope is focused on its area of interest, a series of scans is performed which determine the background brightness before the real search begins. Once this is accomplished, a procedure called "background rejection" is invoked whereby a composite frame of a given

field-of-view is formed by combining between 5-20 individual scans. The actual number of scans is dependent upon the sky conditions.

The first exposure is somewhat longer and is considered as the map and contains stars, satellites, and noise. The next series of frames are subtracted from the original. Since the satellites moved among the stars during the time between the frames, their images are not erased. Once this series of scans is complete, the image is run through a "streak detection algorithm which attempts to eliminate false targets generated by random noise. This information can then be sent to NORAD in real time (4:470).

Ground-Based Laser Radar

In his 1989 thesis, Flt Lt Davey examined the performance requirements for a ground-based infrared LADAR in order to detect deep-space satellites and compared this performance with that of GEODSS (8). The selection of the IR wavelength over the visible was to allow the system to operate in daylight and under a diverse range of meteorological conditions. Since the system was ground-based, the transmissivity of the atmosphere played a key role in the selection of the laser radar.

The selection of the laser was based on five candidate IR LADARs:

- Nd:YAG @ 1.06 μm
- DF @ 3.8 μm
- Frequency-doubled $^{12}\text{CO}_2$ @ 4.5-5.5 μm
- $^{12}\text{CO}_2$ @ 10.6 μm
- $^{13}\text{CO}_2$ @ 11.1 μm

Through the use of LOWTRAN7 and FASCOD 2 computer codes, the frequency-doubled $^{12}\text{CO}_2$ and the $^{13}\text{CO}_2$ showed the best atmospheric transmission. The detector selected was a IR Focal Plane Array (FPA) of 128 x 128 pixels with a quantum efficiency of 85 percent. The transmitter aperture sizes were limited by loss of phase coherence (0.3 m to

1.0 m) and the receiver aperture was selected based on technology (1.75 m). The transmitter power was chosen as 5 MW for the $^{13}\text{CO}_2$ and 2 MW (40 percent efficiency) for the frequency-doubled $^{12}\text{CO}_2$. Additional factors include a target LADAR cross section of 4 m^2 , probability of detection of 0.95, a probability of false alarm of 1×10^{-4} , obscuration ratio of 0.2, pulse repetition frequency of 300 pps, pulse width of $1 \text{ } \mu\text{s}$, and an optics transmission of 0.85.

Davey defined a 'best' detection case as a LADAR detection of a geosynchronous target at 36,000 km range positioned on the sensor zenith, clear skies and perfect heterodyne alignment. The 'worst' case design was defined as detection of a geosynchronous target located off-boresight at a look angle of 60° , a range of 40,000 km and cirrus clouds. His results showed that with an unmodulated pulse train, the proposed system would not receive enough energy to meet the system requirements. By employing a frequency modulation pulse compression technique and the $^{13}\text{CO}_2$, detection was possible in almost all cases.

Davey addressed the possibility of using a space-based LADAR in his thesis. His calculations were solely based on the same laser transmitter and optics diameters set to 1.4 m. His results show that the desired signal-to-noise- ratio is achieved at a range of 6,000 km but he stated that "further analysis of space-based sensor performance is beyond the scope of this study (8:105)."

This thesis will expand on the work done by Davey. Although Davey assumed a heterodyne receiver would provide better performance, this thesis will investigate both direct detection and heterodyne detection. In addition, the laser selection is not confined due to atmospheric conditions and therefore more laser types are possible. Davey also noted that due to the narrow beamwidth of the laser, the estimated positional accuracy of the target must be known fairly well in order to minimize search time. This is one of the main reasons for examining the use of a combined optical and LADAR detection scheme.

2.4. Space-Based Visible Sensor

The possibility of replacing GEODSS with a space-based visible sensor was examined by Capt Koehler in his 1986 thesis (22). In his study, Koehler selected the Defense Meteorological Satellite Program (DMSP) series as a host satellite for the space-based sensor. This satellite is in a circular 833 kilometer near-polar sun-synchronous orbit. The main purpose in using a host satellite was to maintain low cost. This selection of this host satellite was due not only to its orbit, but also to its Precision Mounting Platform, available space, and power.

The optics selected had a diameter of 10 inches and an assumed transmission of unity. The proposed system used a CCD detector with the following characteristics:
(22:33)

• Pixel Size	-	15 - 30 μm
• No. of Pixels	-	800 x 800
• Avg. Quantum Efficiency	-	.61
• Spectral Bandpass	-	.40 - .96 μm
• Operating Temp	-	200 K

The results of the study showed no gain in target detection capability using the satellite-based system over GEODSS but the satellite system would provide a much greater availability.

Capt. Koehler's thesis provides much of the required information for classifying the capability of GEODSS as well as the visible background radiation. Although the visible portion of the proposed combined system will resemble that of Koehler, the size of the optics will most likely be much larger and the sensitivity, therefore, should be greater. As well, the actual optical design will be investigated in order to determine which type of

optical system provides the best performance. Finally, this thesis will also address the problem of satellite attitude and position which are required for updating the element set (ELSET).

2.5. Space-Based Multi-Spectral Sensor

A 1991 study by Lincoln Laboratory, Massachusetts Institute of Technology, proposed using the visible sensor from a Strategic Defense Initiative Organization (SDIO) program (the Midcourse Space Experiment, or MSX) in support of the space surveillance mission. The MSX is a SDIO technology demonstration which is scheduled to fly in late 1993. Its baseline sensors include a Space-Based Visible (SBV) sensor built by MIT/LL. The SBV sensor is designed to demonstrate the feasibility and utility of an above-the-horizon surveillance capability from a space platform, using a broadband visible wavelength detector and signal processor to automatically detect the reflected sunlight from space objects (10:42).

MIT proposes to combine the SBV sensor with a MWIR detection sensor to provide space surveillance both in sunlight and earth shadow. The Multi-Spectral Space Surveillance system would be composed of four to six satellites at low altitude in order to provide real time coverage of orbital space out to geosynchronous altitudes. The visible sensor consists of 8-inch (200-mm) diameter optics with a $1.1^\circ \times 10.8^\circ$ field-of view and a 420×420 back-illuminated CCD focal plane array (23:220). The quantum efficiency versus wavelength for the CCD is shown in Figure (2-2).

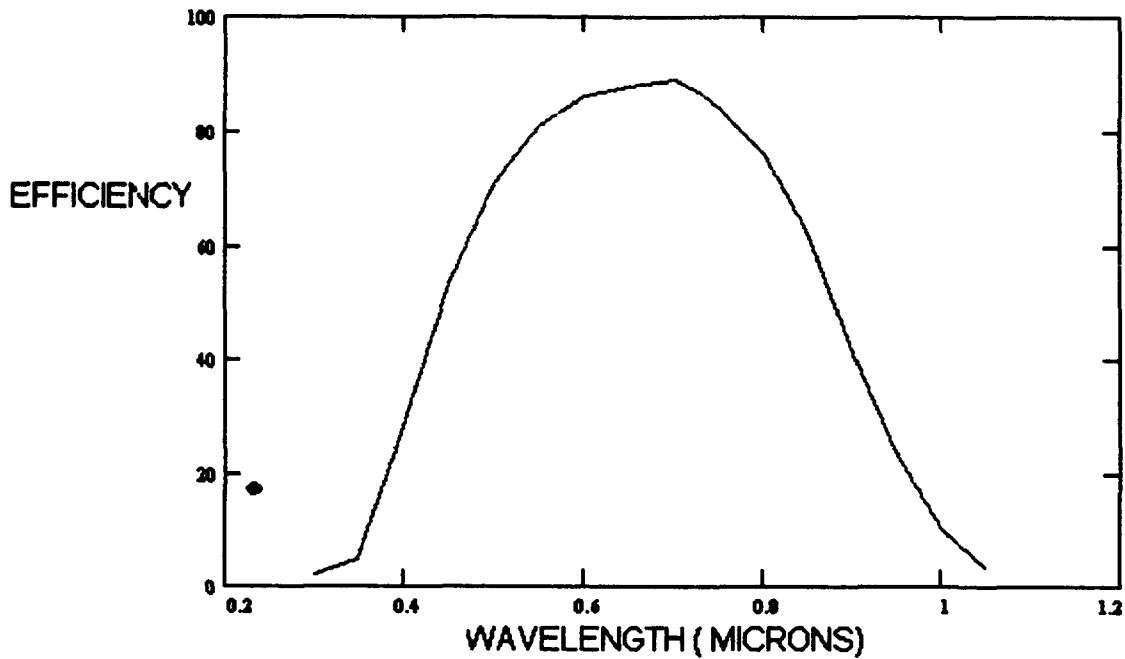


Figure 2.2 Quantum efficiency of back-illuminated imager

Although this technique appears viable, the detection scheme is strictly passive and, therefore, no range or range rate information can be measured. This degrades the accuracy of the orbital element set that is generated. By combining the visible technology (CCD array) with an active technology (LADAR), the sensor could provide not only earth shadow coverage, but range and range-rate information as well.

III. Optical Detection

Introduction

Optical detectors convert an incoming electromagnetic field to an electrical current. They are typically square-law devices which means they produce an electrical current proportional to the incident energy of the field and not its amplitude (20:27). In the case of ideal photon detector (one that produces no output current in the absence of incident power and no noise except that related to the randomness of the emission lines of the photoelectrons) illuminated by monochromatic radiation of frequency ν and constant power P_{sig} the average number of photons occurring in time T is given by (5:128)

$$\overline{N} = \frac{\eta P_{sig} T}{h\nu} \quad (3-1)$$

where

- \overline{N} = average number of photoelectrons
- η = detector quantum efficiency
- P_{sig} = average incident optical power in watts
- T = period of interest
- h = Planck's constant (6.6254×10^{-34})
- ν = frequency of interest

The probability distribution of the photon detection process is given by the Poisson distribution (5:129) (14:13) (20:29). The probability of detecting n photoevents in a given time interval T is

$$P_{\bar{N}}(n) = \frac{\bar{N}^n}{n!} e^{-\bar{N}} \quad (3-2)$$

where

$P_{\bar{N}}(n)$ = probability of n photoevents in time interval T given an average rate of \bar{N} photoevents per time interval T

\bar{N} = average number of photoevents detected in the time interval T

n = number of photoevents in any time interval T

Signal-to-Noise Ratio

One of the key figure of merits for an optical receiving system is the signal-to-noise ratio. This ratio can be expressed either in terms of a ratio of the average photocurrent produced by the signal to the average photocurrent produced by the noise or as a ratio of the received power of the signal to that of the noise. For the purposes of this thesis, the latter will be used and signal-to-noise ratio is defined as (14:16)

$$SNR = \frac{i_{sig}^2}{i_{sn}^2 + i_{th}^2 + i_{bk}^2 + i_{dk}^2 + i_{lo}^2} \quad (3-3)$$

where

i_{sig}^2 = mean square signal current

i_{sn}^2 = mean square shot noise current

i_{th}^2 = mean square thermal noise current

i_{bk}^2 = mean square background noise current

i_{dk}^2 = mean square dark noise current

i_{lo}^2 = mean square local oscillator noise current

In order to calculate this ratio, the noise sources and their statistical distributions must be determined.

Shot Noise (Photon Noise)

Noise is the random fluctuations in the electrical signal from the detector. One source of this noise is the intrinsic variations in the received radiation itself. As stated earlier, the arrival of the photons follow a Poisson distribution. In a photon detection system, the average photocurrent produced is (5:131)

$$i_{sig} = \frac{q\bar{N}G}{T} \quad (3-4)$$

where

q = electron charge (1.602×10^{-19} coulombs)

\bar{N} = average number of photoevents

T = time period of interest

G = gain of the system

A measure of the noise in the photocurrent is the variance of i_{sig} and is given by (5:132)

$$i_n^2 = 2qi_{sig}BG \quad (3-5)$$

where

i_n^2 = total noise power

B = electrical bandwidth $\left(\frac{1}{2T}\right)$

This noise is caused by the variation in the occurrence of the photoevents. Therefore, given a constant signal and no other noise sources, noise is introduced to the system by the arrival of the signal itself. This noise (given no fluctuations in signal power) is referred to as photon or shot noise (5:132).

In the case of a received optical signal power P_{sig} , the average signal current is given by substituting Equation (3-1) into Equation (3-4) (5:134)(14:18)

$$i_{sig} = \frac{\eta q P_{sig} G}{h\nu} \quad (3-6)$$

and applying Equation (3-5); the mean square shot noise is (5:134) (14:18)

$$i_{sn}^2 = \frac{2\eta q^2 P_{sig} B G^2}{h\nu} = 2q P_{sig} \rho_i B G \quad (3-7)$$

where

$$\rho_i = \text{detector responsivity} = \frac{G\eta q}{h\nu}$$

$$G = \text{detector gain}$$

Thermal Noise (Johnson Noise or Nyquist Noise).

The thermal agitation of electrons contained in a resistor will result in voltage fluctuations across the leads of that resistor. If a second resistor is connected across the first one, a fluctuating current will result which is the source for what is called thermal noise. The mean square value of this thermal noise is (20:323)

$$i_{th}^2 = \frac{4kT_{det}BNF}{R_d} \quad (3-8)$$

where

- k = Boltzman's constant ($1.38 \times 10^{-23} \text{ J K}^{-1}$)
- T_{det} = detector temperature
- R_d = detector resistance
- NF = is the noise factor of the receiver following the detector

The power of the thermal noise is directly proportional to the temperature of the detector and, therefore, can be reduced by cooling the detector.

Background Noise.

The photons from the background will cause fluctuations in the carrier or electron densities of the detectors. The result of these fluctuations contributes to the system's shot noise. The mean square background noise can be written using Equation (3-7) (14:17)

$$i_{b_s}^2 = 2qP_{b_s} \rho_i BG \quad (3-9)$$

where P_{b_s} is the power of the background noise.

Dark Noise.

In the absence of photons, the current flowing in the detector is called detector dark current (14:17). This current is device dependent and is caused by such things as leakage current from diodes or thermal excitation of electrons in photomultipliers. Like the background noise, the fluctuations in this current act as shot noise. The mean square dark current noise can be written as (20:379)

$$i_{dk}^2 = 2qI_{dk}BG^2 \quad (3-10)$$

where I_{dk} is the dark current in the detector.

Local Oscillator Noise

The main purpose of the local oscillator in a detection system is to provide a mixing signal for the heterodyne receiver. Like the background noise, the photoelectrons from the local oscillator will act as shot noise on the system and may, therefore, be expressed as (14:17)

$$i_{lo}^2 = 2qP_{lo}\rho_i BG \quad (3-11)$$

The local oscillator is only used for coherent detection and, therefore, this noise term is only relevant when using that detection technique.

Detection Techniques

The detection of both RADAR and LADAR signals is normally described using two parameters - probability of detection (p_d) and probability of false alarm (p_{fa}). The probability of detection is the probability of correctly detecting the return energy of a target while the probability of a false alarm is the probability of mistaking the noise in the system as a target. The determination of these parameters is derived from the statistical nature of the signal and noise sources. Although the signal return from the target may be identical for both coherent and incoherent detection, the statistics for the noise in each case is different. Therefore, both detection techniques must be examined separately.

Coherent Detection

In a coherent system, the return laser pulse is heterodyne detected and then passed through a matched filter. The output from this filter is then envelope detected and compared against a predefined threshold. The threshold is set from the noise power and the desired probability of false alarm. If the output from the envelope detector is above the decision threshold, a target is said to have been detected.

In order to achieve nearly quantum-noise-limited detection with a heterodyne receiver, the local oscillator is adjusted to make the local-oscillator-induced shot noise the dominant noise source in the system. This allows us to ignore the unpredictable background noise source and model the resultant photocurrent using Gaussian statistics (3:39). The noise current can be represented using complex notation as (8:55):

$$n(t) = r(t)e^{j\phi(t)} \quad (3-12)$$

where

$n(t)$ = the time-dependent noise current

$r(t)$ = the amplitude of $n(t)$

$\phi(t)$ = the phase of $n(t)$

The joint probability density function of $r(t)$ and $\phi(t)$ is then given by (3:39)

$$p(r, \phi) dr d\phi = \frac{r}{2\pi\sigma_n^2} e^{-\frac{r^2}{2\sigma_n^2}} dr d\phi \quad (3-13)$$

where

$p(r, \phi)$ = joint probability density function of the noise current

σ_n = average noise power

The average noise power is determined from Equation (3-11) as the local oscillator is the dominant source of noise. Since the envelope detector is insensitive to the ϕ dependence, it can be integrated out resulting in a Rayleigh-distributed probability density function (8:55)

$$p(r) = \frac{r}{\sigma_n^2} e^{-\frac{r^2}{2\sigma_n^2}} \quad (3-14)$$

The probability of the return being a false alarm is equal to the probability that the output exceeds the decision threshold bias (r_b). The p_{fa} may then be given by (3:40)

$$p_{fa} = \int_{r_b}^{\infty} p(r) dr = e^{-\frac{r_b^2}{2\sigma_n^2}} \quad (3-15)$$

where r_b is the decision threshold voltage.

Normally, most users are more concerned with the time between false alarms (T_{fa}) which is given by (35:25)

$$T_{fa} = \frac{1}{B_{IF}} e^{\frac{r_b^2}{2\sigma_n^2}} = \frac{1}{p_{fa} B} \quad (3-16)$$

where B_{IF} is the IF bandwidth of the envelope detector. Due to the exponential relationship between the threshold value and the time between false alarms, a small change in the threshold voltage results in a large change in the time between false alarms.

When determining the probability of detection (p_d), the output of the envelope detector consists of both the signal and the noise. In general, satellites are modeled as hybrid targets containing both diffuse and specular components (8:16). Without knowing the relative contributions of the components, it is not possible to know precisely the probability density function of the return signal.

It has been shown that targets with a comparatively small amount of diffuse signal have a distribution that more closely resembles a purely diffuse target (3:43). Therefore, in order to simplify calculations, this thesis will assume the satellites to be diffuse targets. A diffuse target normally produces a scattered field of bright and dimmed spots known as speckle. This is caused by the interference effects of the randomly positioned individual scatterers. Each of these scatterers contributes to the electric field. This results in a return signal composed of a sum uniformly distributed random phase signals. As long as the number of individual scatters is large (>30), by use of the Central Limit Theorem, the photocurrents produced by this field will have independent Gaussian distributions with a common variance and zero mean. Since both the noise and the signal components have Gaussian distributions, the sum of these signals will have a Gaussian distribution with a variance equal to the sum of the variances of the noise and the signal. This sum is the output of the envelope detector and has a Rayleigh distribution given by (3:40)

$$p(r') = \frac{r'}{\sigma_t^2} e^{-\frac{r'^2}{2\sigma_t^2}} \quad (3-17)$$

where

- r' = the combined amplitude output of signal and noise
- σ_t^2 = the sum of the variances of the noise and signal ($\sigma_n^2 + \sigma_s^2$)
- σ_s^2 = the average signal power from a diffuse target

The sum of the variances can now be related to the diffuse signal-to-noise ratio (SNR) by the following expression

$$\sigma_i^2 = \sigma_n^2 (1 + \text{SNR}) \quad (3-18)$$

where $\text{SNR} = \frac{\sigma_s^2}{\sigma_n^2}$

As with Equation (3-15) earlier, the probability of detection can be written as

$$p_d = \int_{\gamma}^{\infty} p(r') dr' = e^{\frac{-\gamma^2}{2\sigma_i^2}} \quad (3-19)$$

By combining Equations (3-15), (3-18), and (3-19), the relationship between SNR, p_d and p_{fa} can be shown as (3-20)

$$p_d = (p_{fa})^{1/(1+\text{SNR})} \quad (3-20)$$

From this equation, it can be seen that by specifying a probability of false alarm (or time between false alarms) and a probability of detecting a target, results in a minimum SNR to achieve these parameters. Then, by using Equation (3-3), the SNR can be related to the power of the signal and noise of the detection system.

Incoherent Detection (Direct Detection or Energy Detection)

For the incoherent detection system, the signal is assumed to be a rectangular pulse since this type of waveform is relatively simple and is the optimum choice for low signal-to-noise ratios (3:17). The receiver consists of energy-collecting optics, an optical filter to reduce background radiation, a photodetector, photoelectron processing circuits, and a decision apparatus. The received energy from the background and signal generates photoelectrons modeled using Poisson statistics. These photoelectrons are counted for an interval equal to the pulse duration and associated with a particular range cell. The result of this cell is presented to the decision apparatus to determine if the threshold voltage has been crossed indicating the presence of a target.

In the case of incoherent detection, there is no local oscillator generating high numbers of photoelectrons. Incoherent systems typically have a lower photon count and, therefore, must be modeled using Poisson statistics. From Equation (3-2), the probability of generating n noise photoelectrons in an interval is given by (3:20)

$$p_n(n) = \frac{(\bar{N}_n)^n}{n!} \exp(-\bar{N}_n) \quad (3-21)$$

For incoherent detection, \bar{N}_n is average number of noise photoelectrons emitted per counting interval due to thermal noise, dark current and external-noise sources and is given by

$$\bar{N}_n = \sqrt{(i_{th}^2 + i_{bk}^2 + i_{dk}^2)} \left(\frac{T}{q} \right) \quad (3-22)$$

A target whose illuminated region is a small portion of the resolution cell is called not resolvable. The signal photoelectrons for a diffuse target that is not resolvable obey Bose-Einstein statistics and the probability of generating n signal and noise photons is given by (3:22)

$$p_{s+n}(n) = \frac{\exp(-\bar{N}_s)}{1 + \bar{N}_s} \sum_{j=0}^n \frac{(\bar{N}_s)^j}{j!} \left(\frac{\bar{N}_s}{1 + \bar{N}_s} \right)^{n-j} \quad (3-23)$$

where

$p_{s+n}(n)$ = the probability of receiving k signal and noise photoelectrons
 \bar{N}_s = the average number of signal photoelectrons emitted is defined in Equation (3-1)

Given these formulas, the p_{fa} and p_d can be calculated. If p_{fa} represents the maximum tolerable false-alarm probability in any given range cell, then the probability of accumulating sufficient noise photoelectrons to cross the threshold voltage is given by the minimum integer satisfying (3:18)

$$p_{fa} \geq \sum_{n=N_t}^{\infty} p_n(n) \quad (3-24)$$

where

p_{fa} = the probability of false alarm
 N_t = the threshold number of photoelectrons required to cross the threshold set for detection of a target

Similarly, the probability of detection is the probability of receiving the minimum number of required signal and noise photoelectrons to indicate a detection (Probability ($n \geq N_t$)) and is given by (3:20)

$$p_d = \sum_{n=N_t}^{\infty} p_{s+n}(n) \quad (3-25)$$

A large load resistor combined with sufficient cooling can usually ensure a detector is not limited by thermal noise. If this is the case, then by using Equations (3-3), (3-4), (3-5), and (3-22) the relationship between the average number of noise and signal photoelectrons and SNR is given by

$$SNR = \frac{\frac{\bar{N}_s^2 q^2 G^2}{T^2}}{\frac{2\bar{N}_s q^2 G^2 B}{T} + \frac{\bar{N}_s q^2}{T^2}} \quad (3-26)$$

The number of noise photoelectrons is determined from a radiometric study of the background noise combined with internal noise generated by the detector itself. From a given probability of false alarm and the number of noise photoelectrons, a threshold voltage is determined. Then, for a given probability of detection, the number of signal photoelectrons required to achieve the specified p_d is determined. These values can then be used in Equation (3-26) to determine the required SNR to achieve the performance.

For a detector with a gain equal to 1 and a bandwidth set to $1/(2T)$, the SNR expression reduces to a simple quadratic formula given by

$$\bar{N}_s^2 - (SNR)(\bar{N}_s) - (SNR)(\bar{N}_s) = 0 \quad (3-27)$$

whose solution is given as

$$\bar{N}_s \geq \frac{SNR + \sqrt{SNR^2 + (4)(SNR)(\bar{N}_s)}}{2} \quad (3-28)$$

A plot of SNR versus detection probability for various values \bar{N}_s and a p_{fa} of 1×10^{-6} is shown in Figure (3-1) (3:21).

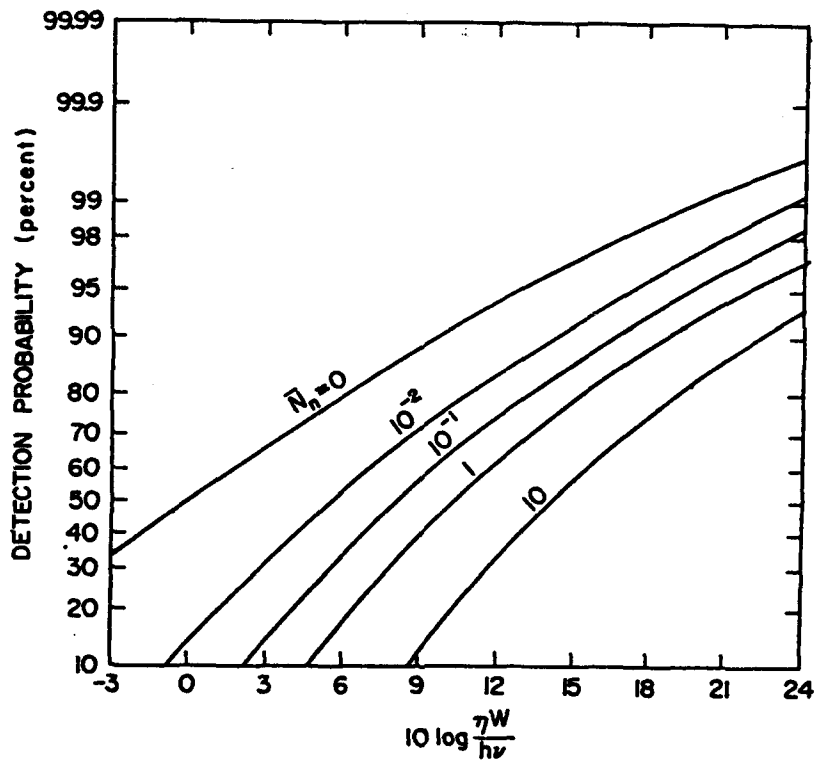


Figure 3.1 Detection Statistics - Incoherent Detection of Nonresolved Tough Target

Comparison of SNRs of Coherent and Incoherent Systems.

SNR of Coherent Systems

In the analysis of the coherent system, two parallel plane waves (local oscillator and signal) are assumed to be incident on a detector whose quantum efficiency is η and area is A . The field at the detector can then be written as (18:24)(5:197)

$$E_{inc}(t) = E_{lo} \cos \omega_{lo} t + E_s \cos \omega_s t \quad (3-29)$$

where

E_{lo} = local oscillator field

E_s = signal field

ω_{lo} = frequency of the local oscillator

ω_s = frequency of the signal

and the power incident on the surface may be written as (18:24)(5:197)

$$P_{inc}(t) = \frac{E_{inc}^2(t) A}{z_o} \quad (3-30)$$

where z_o is the impedance of free space. Using Equation (3-6) for the current signal, it can be shown that the resulting photocurrent is given by (18:25)(5:197)

$$i(t) = i_{lo} + i_s + 2\sqrt{i_{lo} i_s} \cos(\omega_s - \omega_{lo})t \quad (3-31)$$

The mean square intermediate frequency (i.f.) current at frequency $(\omega_s - \omega_{lo})$ is the signal portion measured by the envelope detector and is given by (18:25)(5:198)

$$\overline{i_{i.f.}^2} = \frac{(2\sqrt{i_o i_s})^2}{2} = 2i_o i_s \quad (3-32)$$

For the purposes of this comparison, it is assumed that the noise of the coherent detection system is dominated by the shot noise of the local oscillator. Using Equation (3-5), Equation (3-11), and then Equation (3-6), the power signal-to-noise ratio for a coherent detection system can be expressed as (18:25)

$$SNR_p = \frac{\overline{i_{i.f.}^2}}{i_n^2} = \frac{2i_o i_s}{2qP_o \rho_i BG^2} = \frac{2i_o \left(\frac{\eta q P_{sig} G}{h\nu} \right)}{2q \left(\frac{i_o h\nu}{\eta q G} \right) \rho_i BG^2} = \frac{\eta P_{sig}}{h\nu B} \quad (3-33)$$

where B is the electrical bandwidth of the receiver. This Equation shows that the signal-to-noise ratio for a coherent system is directly proportional to the power of the received signal and is not affected by the power introduced by the local oscillator. The value of the SNR required for this Equation is determined from Equation (3-20).

SNR of Incoherent Systems

While the signal-to-noise ratio for the coherent detection system is directly proportional to the power of the received signal, the incoherent system depends on the received signal power and the relative magnitudes of the power of the contributing noise sources. Using Equations (3-3), (3-6), (3-7), (3-8), and (3-9) the signal-to-noise ratio of an incoherent detection system can be expressed as

$$SNR = \frac{\eta P_{sig}^2 G^2}{h\nu 2BG^2(P_{sig} + P_{bg}) + \frac{h^2\nu^2}{\eta q^2}(G^2 P_{dk} + P_{th})} \quad (3-34)$$

where

P_{sig} = power of the received signal

P_{bg} = power of the background noise

P_{dk} = equivalent dark current power = $\frac{A_d B}{(D^*)^2}$

D^* = specific detectivity = $\frac{\sqrt{A_d B}}{P_N}$

A_d = area of the detector

P_N = Noise Equivalent Power = noise current/responsivity = $\frac{i_n}{\rho}$

P_{th} = equivalent receiver thermal noise = $\frac{4kTBNF}{R_d}$

This SNR expression is identical to Equation (3-26) except that the thermal noise in Equation (3-26) has been disregarded.

The performance of an ideal detector can be evaluated by eliminating all noise sources. This performance is referred to as signal-noise-limited detection or photon-limited detection. The only noise in the detection system is a result of the photon noise generated from the received signal power. From Equation (3-34), the signal-to-noise ratio for photon-limited detection is given by

$$SNR_{photon} = \frac{\eta P_{sig}}{2h\nu B} \quad (3-35)$$

When this Equation is compared to Equation (3-33) then, even in the absence of background signal, the incoherent detection technique can only produce a power SNR that is one-half that of the coherent technique. While this seems to favor using a coherent detection system, it is important to remember that for a given probability of false alarm and probability of detection, the coherent system will require a higher signal-to-noise ratio in order to achieve the detection at low signal levels due to the larger noise variance caused by the variance in the signal itself as well as the variance of the envelope detector. A comparative performance of the two detection techniques is shown in Figure (3-2) (3:23).

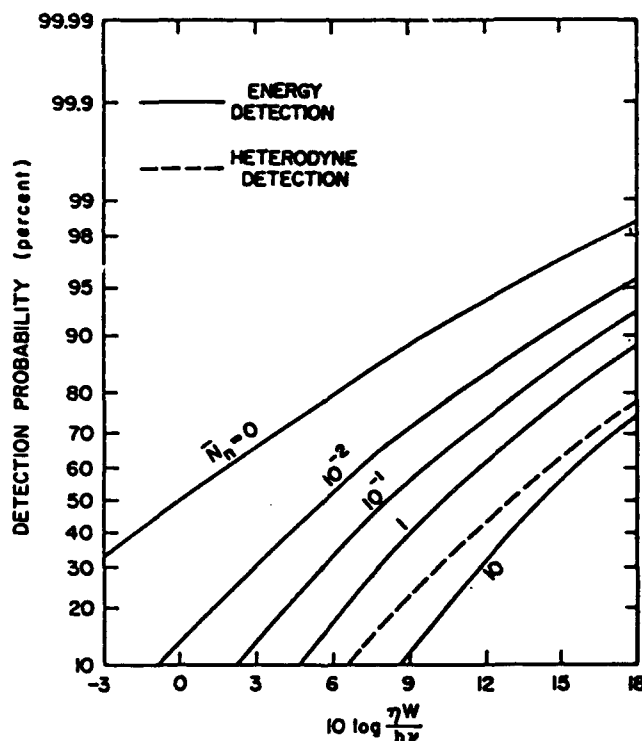


Figure 3.2 Comparative performances of heterodyne and energy detection - nonresolved target

In the cases where one noise dominates in the system, then using Equation (3-34) we can express the limited SNRs as

$$SNR_{background} = \frac{\eta P_{sig}^2}{2h\nu BP_{bg}} \quad (3-36)$$

$$SNR_{thermal} = \frac{\eta^2 G^2 q^2 R P_{sig}^2}{h^2 \nu^2 4kTBNF} \quad (3-37)$$

$$SNR_{dark} = \frac{\eta^2 q^2 (D^*)^2 P_{sig}^2}{h^2 \nu^2 A_d B} \quad (3-38)$$

The SNRs for both coherent and incoherent detection depend on the received power from the target. In order to calculate this value, the LADAR range Equation must be used.

Pulse Integration

The relationships between the signal-to-noise ratio, the probability of detection, and the probability of false alarm derived previously apply only for the case of a single pulse return. However, the detection capability can be improved by integrating the returns of many pulses and treating them as a single return. Integration improves the signal-to-noise ratio because signals combine additively, whereas the added noise samples have a fluctuation that is not the direct sum of the added fluctuations. When adding N signal samples of unit amplitude, the sum of the signals (voltage) is equal to N while the sum of the noise samples results in a noise power growing as \sqrt{N} . The improvement in the signal-to-noise ratio (voltage) is \sqrt{N} while the improvement in the signal-to-noise ratio (power) is N (36:2-16).

For incoherent systems, only postdetection is practical and is also the preferred method for coherent systems (36:37-35). The improvement in signal-to-noise using

postdetection is less than N times that of a the single pulse due to nonlinearity of the detector (35:29). The improvement in the signal-to-noise ratio when N pulses are integrated using postdetection is known as the integration-improvement factor ($I_i(N)$). The relationship between this improvement and the number of pulses integrated is given in Figure (3-3) (36:38-36). The top solid line represents the improvement expected from a perfect integrator while the bottom dashed line represents \sqrt{N} improvement. Note that the slope of the line starts as a perfect integrator, but as the number of pulses integrated increases, the slope changes to that of a \sqrt{N} improvement. (Note: n_f is equal to $1/p_{fa}$)

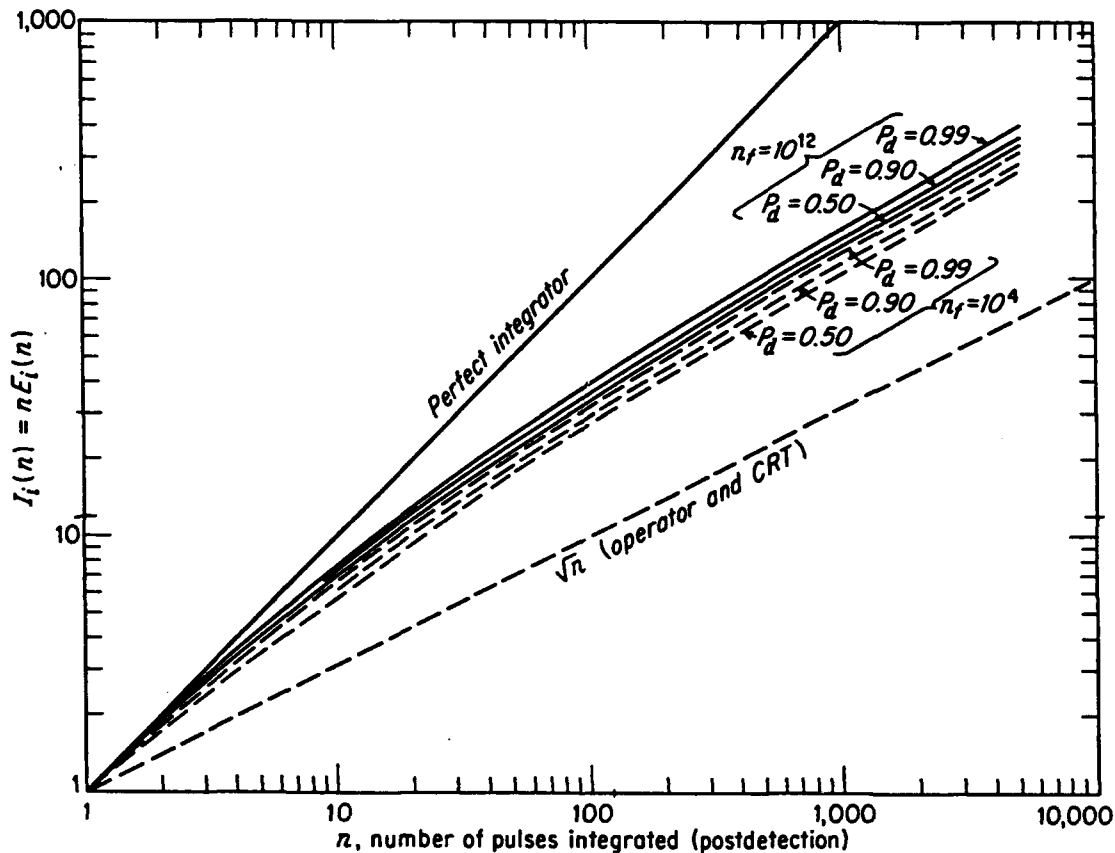


Figure 3.3 Integration efficiency as a function of number of pulses integrated.

In addition to the increase in signal-to-noise ratio, the integration of pulses also has an effect on the probability of false alarm since decisions on the presence or absence of targets are made less often. For a pulsed system using range gates the time between false alarms is given by (36:2-17)

$$t_{fa} = \frac{N\tau_g}{p_{fa}(1-\delta)} \quad (3-39)$$

where

- N = number of pulses integrated
- τ_g = gate "on" time
- δ = time that no gates are open

LADAR Range Equation

In order to determine the signal-to-noise ratio of any proposed system, the amount of power received must be determined. This is calculated using the LADAR range equation. There are several versions of this equations but all are basically the same. For this thesis, the equation from Jelalian will be used (14:3)

$$P_{sig} = \frac{P_t G_t \sigma \pi D^2 \eta_{sys}}{64\pi^2 R^4} \quad (3-40)$$

where

- P_{sig} = received signal power in watts
- P_t = transmitter power in watts

The receiver provides a gain to the signal and then the final term is to compensate for the efficiency of the system.

System Efficiency (η_{sys})

The efficiency term is used to incorporate performance limitations such as those due to optics transmission, target reflectivity, target polarization, phase front alignment, receiver/processor loss, transmitter efficiency, and receiver efficiency. Some of these parameters, such as receiver/processor loss and target polarization, are specific to a particular system design and/or target characteristics. For this thesis, the system efficiency term is simply the product of the optics transmission (η_{O}), transmitter efficiency (η_{t}), and the receiver efficiency (η_{r}). Target reflectivity is accounted for in the assumption of the target size.

Optical Transmission (η_{O})

The efficiency of the optics is determined by the percentage of the in-band frequency incident on the optics. Losses can occur if the field stop of the system is not the front lens. In addition, if the reflectivity of the mirrors or transmissivity of the optics is not 100 percent, then the reflecting or refracting surfaces will decrease optical transmission. The decrease in optical transmission due to obscuration will be accounted for in the transmitter and receiver efficiencies.

Transmitter Efficiency (η_{t})

The transmitter antenna efficiency accounts for losses caused by a finite antenna aperture, obscuration by secondary elements and diffraction effects in the radiated pattern. This problem was examined by Klein and Degnan (20:2134) and they found that for an unobscured aperture, the maximum gain is simply a function of the primary aperture radius

divided by the beamwidth (Note: beamwidth defined at the $1/e^2$ point). Their calculations showed that the maximum gain occurs on-axis for an aperture radius (a)-to-beam radius (ω) ratio of 1.12. This means that the laser transmitter is not fully beam expanded to cover the entire aperture in order to maximize the gain. The corresponding efficiency factor (η) of this maximum gain is 0.8145.

For non-zero values of obscuration (γ), Klein and Degnan used second-order perturbation theory to determine the optimum aperture to beamwidth ratio for a general obscuration. The far-field on-axis efficiency (of three different obscuration ratios) is illustrated in Figure (3-4). The graph shows how the efficiency decreases as the size of the obscuration increases. The graph also depicts the steep decline in efficiency when the optimum aperture to beamwidth ratio is not selected.

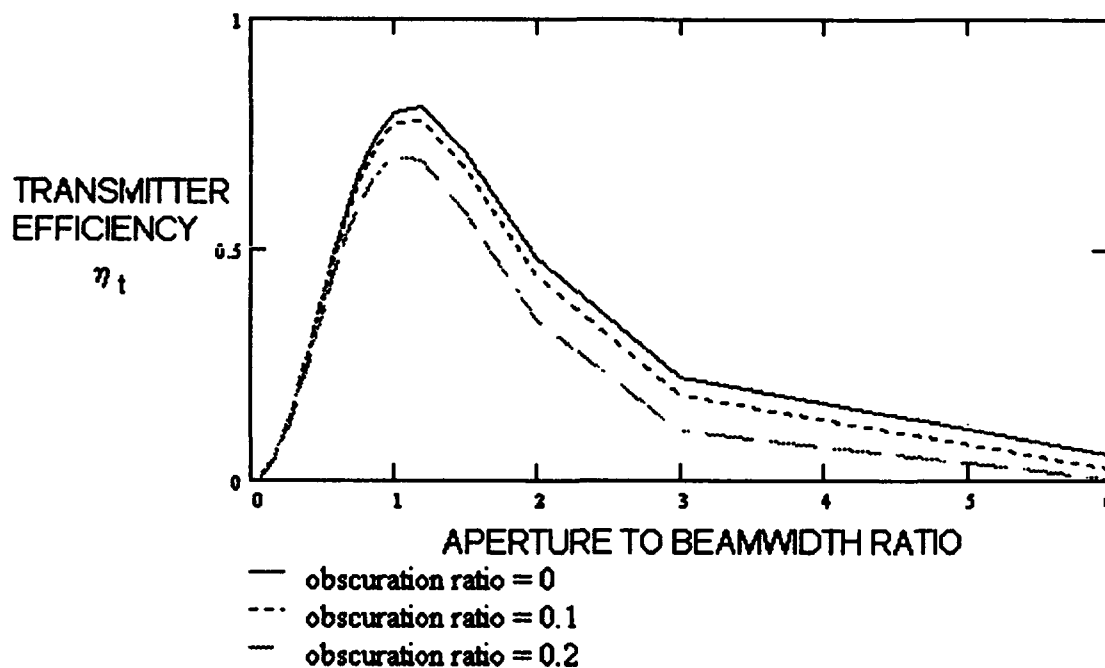


Figure 3.4 Far field on-axis efficiency as a function of obscuration ratio and aperture to beamwidth ratio

Knowing that the power of the transmitted beam will decrease as a function of increased distance from the center, it is expected that the transmitter efficiency should decrease as distance off-axis is increased. This relationship is shown by using an off-axis plotting parameter X ($X = k a \sin \theta$). This off-axis parameter is plotted as a function of obscuration ratio and transmitter efficiency in Figure (3-5). The wavelength selected is $1.06 \mu\text{m}$ which corresponds to the wavelength of a Nd:YAG laser. The aperture diameter is arbitrarily set to 1 meter. As expected, the efficiency decreases as the obscuration ratio increases and as the off-axis parameter increases.

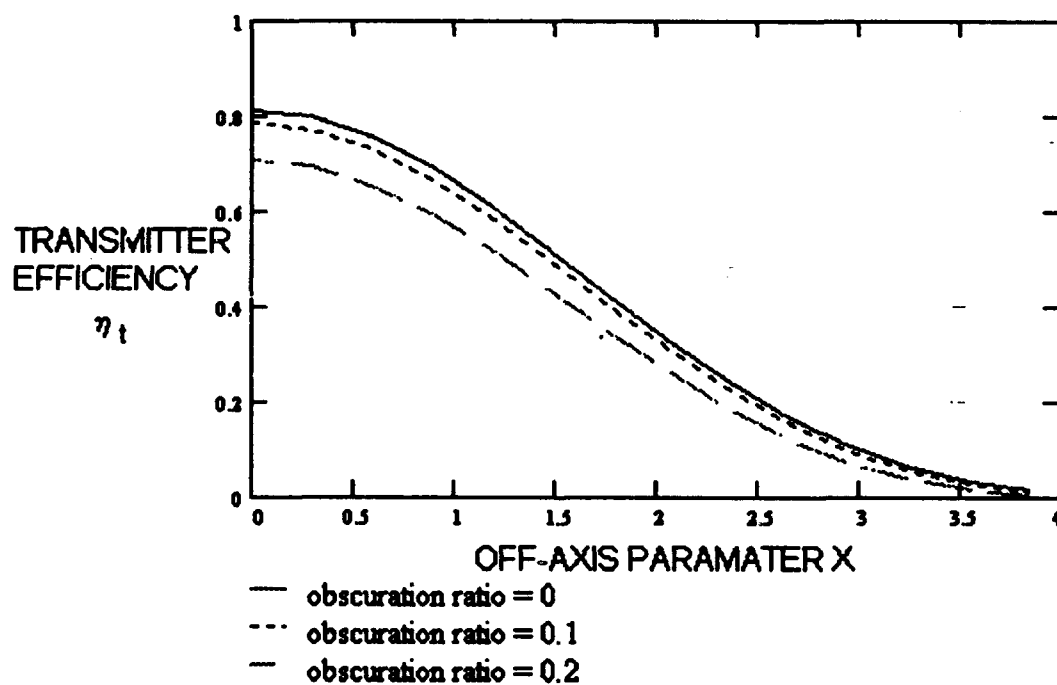


Figure 3.5 Transmitter efficiency as a function of off-axis parameter X

Receiver Efficiency (η_r).

Equation (3-41) for the gain of a receiver is the ideal gain and does not account for blockage of light due to obscuration, spillover of energy beyond the perimeter of a finite

detector, or the effects of the local oscillator distribution in heterodyne and homodyne detection. These losses will be represented in the receiver efficiency term defined as

$$\eta_r = (1 - \gamma^2) \eta_d \quad (3-44)$$

where

η_r = receiver efficiency

γ = obscuration ratio

η_d = efficiency of the detection technique

For the purposes of this analysis, it is assumed that the source is of sufficient distance from the detection system that the incoming energy is in the form of plane waves. The telescope then plays the role of collecting the energy and focusing it to a detector in the rear focal plane. The fraction of the power detected is simply the ratio of the power falling on the detector to the power received by the system. For a direct detection system, Figure (3-6) shows the relationship between receiver efficiency (η_d) at several obscuration ratio's versus σ_d , where

$$\sigma_d = \frac{kR_d}{2F_s}$$

R_d = radius of detector (assumed circular)

$$k = \frac{2\pi}{\lambda}$$

$$F_s = \text{antenna F number} = \frac{\text{effective focal length}}{\text{aperture diameter}} = \frac{f_{eff}}{2a}$$

The curves indicate the decreasing direct detection efficiency with the increase in obscuration ratio or as σ_d decreases. (20:2135)

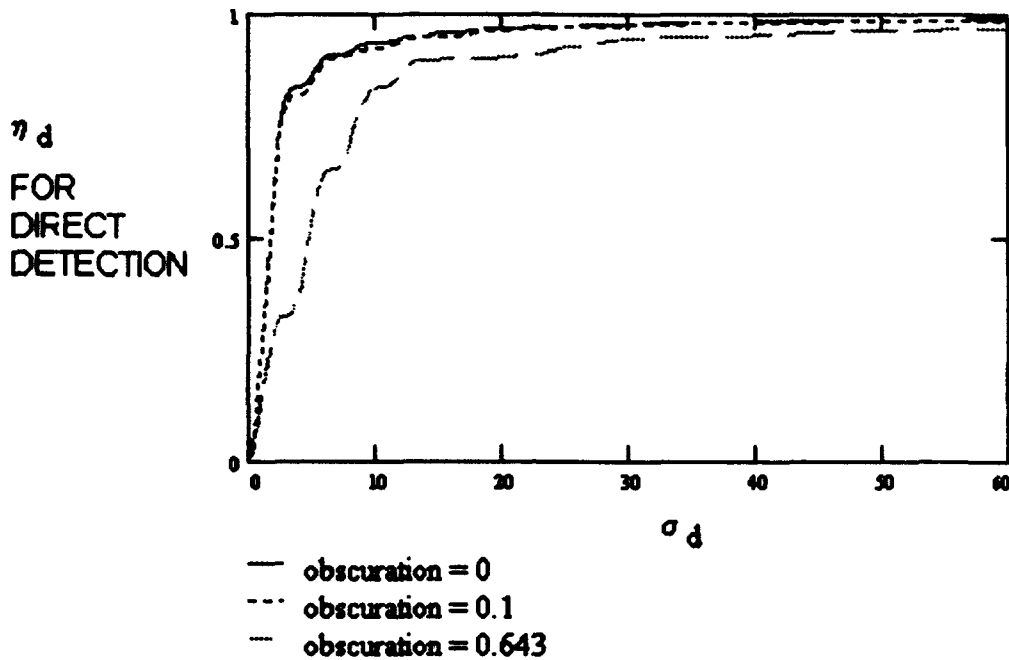


Figure 3.6 Detection efficiency (η_d) of direct detection as a function of obscuration ratio and σ_d

For the heterodyne system, the detection efficiency is dependent on the shape of the local oscillator field distribution and not its magnitude. Degnan and Klein derived the expression for several different distributions of local oscillator fields. For a uniform local oscillator distribution across the detector, the heterodyne efficiency is a function of the Airy spot size (R_a) which is itself is dependent on the obscuration ratio (γ). The quantity σ_h (defined as $\sigma_h = \frac{kR_a}{2F}$), relates the Airy spot size to the wavelength, and antenna F number (20:2399). The relationship between σ_h and obscuration ratio (γ) is shown in Figure (3-7). This graph shows that for a constant F-number at a given wavelength, as the size of the secondary element is increased (i.e., a larger obscuration ratio), the size of the Airy spot decreases.

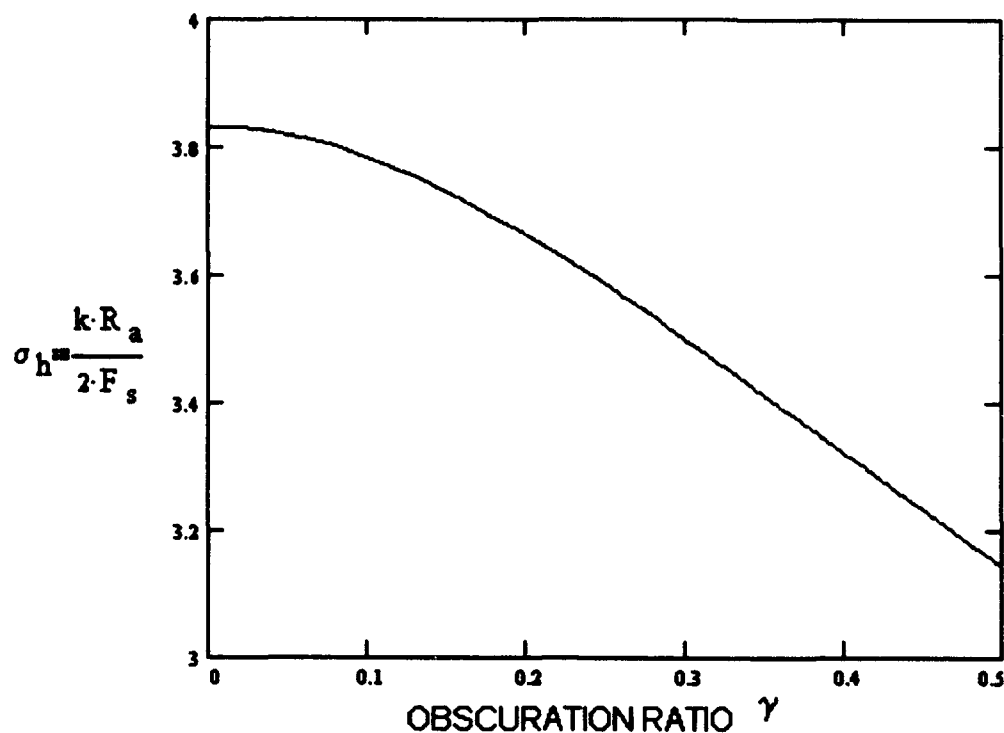


Figure 3.7 Airy spot radius and F-number as a function of obscuration ratio

Heterodyne detection efficiency is plotted in Figure (3-8) as a function of the ratio (defined as r) of detector radius (R_d) to the Airy spot radius (R_a) for several obscuration ratios. The graph depicts the minimum detection loss occurs at $r \approx .75$. The reason for this is that even though the power in the IF signal increases beyond $r = .75$, the noise from the local oscillator increases greater which decreases the overall SNR.

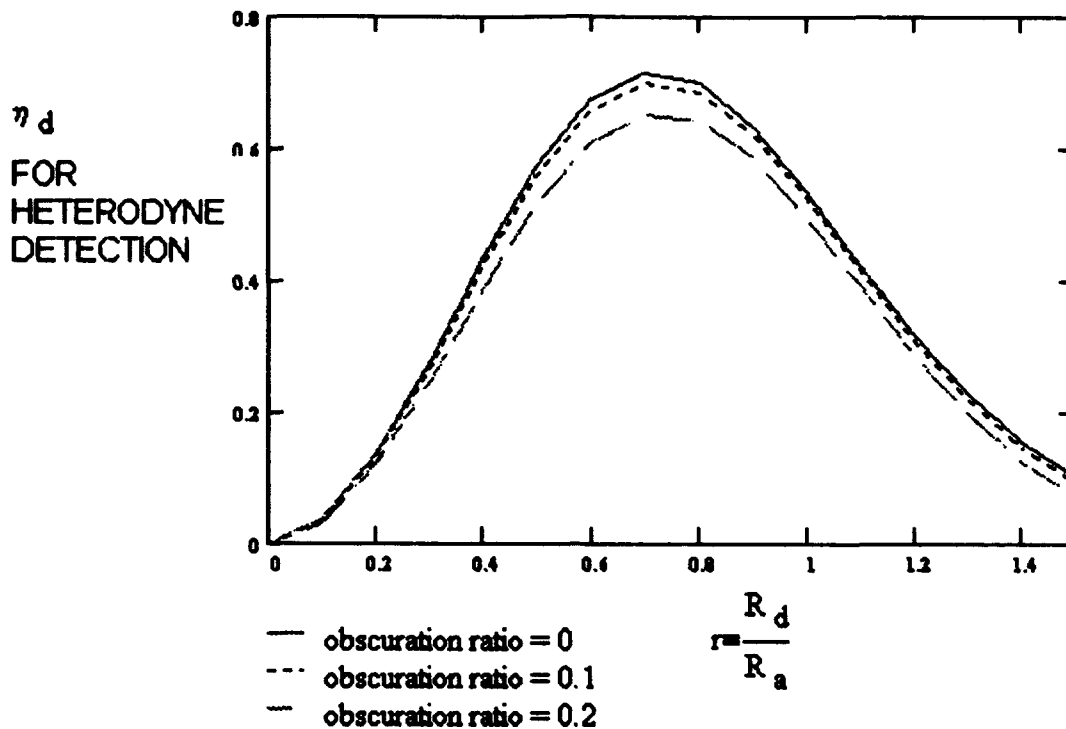


Figure 3.8 Receiver efficiency for uniform local oscillator as a function of the obscuration ratio and the ratio of the detector radius to the Airy spot size (r)

In the case of the Gaussian local oscillator distribution, the heterodyne efficiency is a function of the Airy spot-to-Gaussian local oscillator spot size ratio. Degnan and Klein found that the optimum value of this ratio was 2.2 varied only slightly as a function of the obscuration ratio for $r \leq 1$. The graph in Figure (3-9) shows that as the detector-to-Airy ratio increases above .83, the heterodyne efficiency decreases. As with the uniform distribution, this decrease due to the increased shot noise from the local oscillator. The decrease in efficiency past $r = .75$ is less than for the uniform distribution due to the decrease in intensity of the Gaussian local oscillator. (Note: the efficiency (η) is expressed as a function of the obscuration ratio (γ), the ratio of detector radius to Airy spot radius ratio (r), and the Airy spot-to-Gaussian local oscillator spot size ratio (t .)

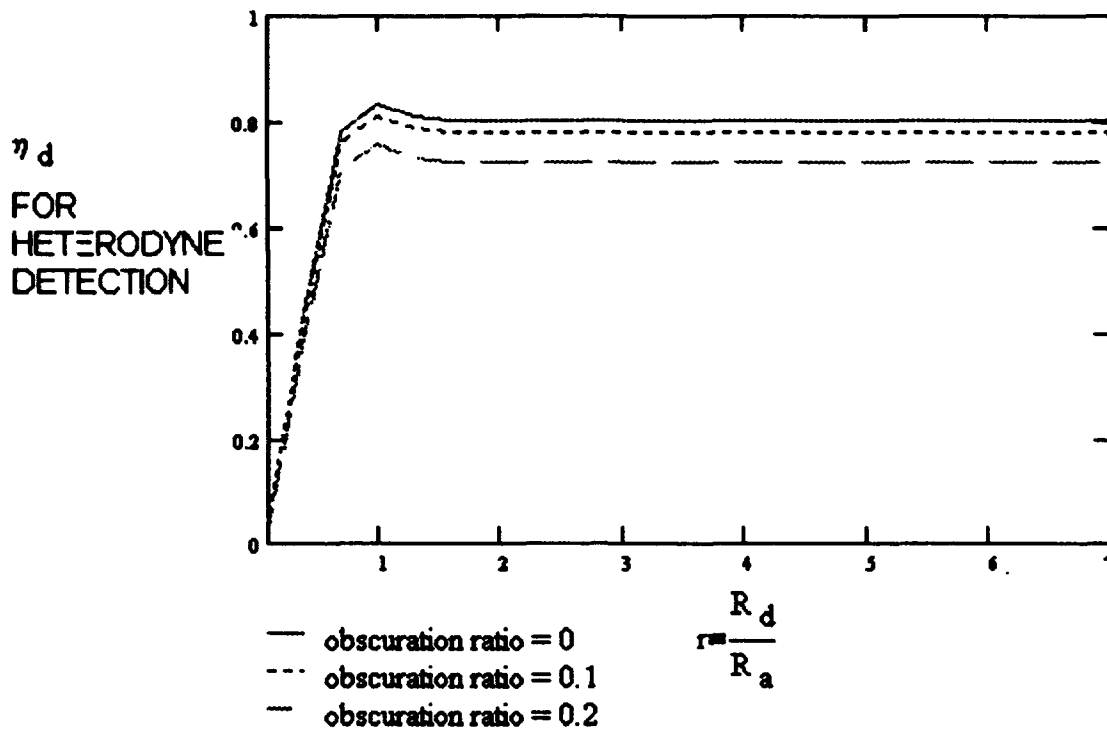


Figure 3.9 Receiver efficiency for Gaussian local oscillator as a function of obscuration ratio and the ratio of the detector radius to the Airy spot radius

A third type of local oscillator distribution is that of a matched oscillator. To achieve this, the local oscillator beam is enlarged and then focused through a centrally-obscured lens which has a clear aperture that is small compared to the enlarged beamwidth. By choosing the F number of the focusing optics and the size of the central obscuration relative to the clear aperture the beam can be optically matched to the signal beam. The heterodyne efficiency in this case is identical to that of direct detection and is plotted in Figure (3-6). Depending on the obscuration ratio and detector radius, the extra difficulty in matching the wavefront may not provide much added efficiency. Therefore, for the efficiency versus complexity, this thesis will assume a Gaussian local oscillator is being used.

IV. System Components and Design

Introduction

The selection of system components and design for a space-based LADAR system is complicated by the fact that no such system has been tested in a space environment. The development of space-based LADAR systems has been limited to mainly three applications: atmospheric remote sensing, optical space communications, and SDI programs for missile detection. The selection of components for the deep-space LADAR system is based upon the current component technology of these three applications. This chapter will describe the components selected as well as additional factors that must be considered in the system design.

Laser Transmitters

The choice of candidate laser transmitters to evaluate were selected from the most promising technologies for space-based optical communications. With the key requirements for the system being high power, mature technology, and good transmitter efficiency, four transmitting technologies were selected. The four systems are based upon the carbon-dioxide gas laser, the neodymium-doped yttrium-aluminum-garnet (Nd:YAG) solid-state laser, the indium-gallium-arsenide (InGaAs) semiconductor diode laser, and the gallium aluminum arsenide (GaAlAs) semiconductor diode laser.

Choosing a transmitter is not as simple as just selecting one that provides the largest output power. Since this system must be integrated into the overall satellite design, whenever possible, selection was based upon transmitters currently being developed for space applications. In most cases, a coherent transmitter, as well as one for direct detection, is selected for each transmitter type. It is assumed that all transmitters are either "space-qualified" or capable of becoming space qualified.

Carbon Dioxide Laser.

Carbon-dioxide laser radar technology is the oldest and the most mature. This LADAR technology is already being used by the Firepond project in order to track low-earth-orbiting targets from the ground. Carbon-dioxide transmitters have the advantage of very high output power in both single and multi-modes. In addition, compared to other technologies, these systems have reduced pointing and tracking requirements because of their relatively large beamwidth (27:29). For the purposes of this thesis, the CO₂ transmitter selected is that being developed under the Strategic Defense Initiative. The transmitter is capable of producing > 7 joules output pulse at a 30 Hz average repetition rate at 10.6 μm (9:3). Since this transmitter is operated in TEM₀₀ mode, it will be used for both the direct and coherent detection analysis.

Nd:YAG Laser.

Nd:YAG laser transmitters provide high power and fairly long lifetime (based on pumping from diode laser arrays) but are the least efficient in terms of energy conversion (typically 4 - 15 percent) (16:159) (21:174). The Nd:YAG transmitter will be used in the first space-qualified laser transmitter to be launched on the Lidar In-Space Technology Experiment in 1994 (STS-65) (15:33). Current technology for these laser transmitters for space applications indicate an average output of 50 W with a pulse repetition frequency (prf) of 40 Hz and a energy of 1.25 joule/pulse is achievable for direct detection purposes and 30 W average output with an energy of .75 joule in a 17-nsec Q-switched pulse is achievable for coherent detection (21:169).

InGaAs Laser.

The increasing output power of diode lasers and the capability to combine stacked arrays to create more powerful sources make diode-based laser radars excellent candidates

for long-range laser radars. Although these transmitters cannot currently match CO₂ or ND:YAG systems for TEM₀₀ single mode output, their multi-mode output compares favorably. One of the main advantages of these systems is their high efficiencies. Wall plug efficiencies of 40 percent have been reported, although 20 to 25 percent is more common (25:31). While diode lasers are not able to achieve the higher peak powers of Q-switched lasers because of the longer pulse widths, their average powers can currently surpass those of Nd:YAG systems.

For direct detection, the Spectra Diode Labs SDL 6231-B6 Quasi CW laser source is selected which provides 360 W peak output power with 144 mJ of energy per pulse and a maximum pulse width of 400 μ sec. This laser is run with a 2 percent duty cycle or 50 Hz and is available in wavelengths from 940 to 980 nm (37:87). For coherent detection, the Spectra Diode Labs SDL 5762-A6 1 watt continuous wave (CW) single mode master oscillator power amplifier (MOPA) Laser Diode is selected. It operates at 985 nm with a 25 percent overall efficiency (37:44).

GaAlAs Lasers.

GaAlAs quasi-CW stacked-array lasers are capable of producing peak powers up to 5 kW in multi-mode operation. The SDL 3251-HK is capable of producing 2 J/pulse with a pulse width of 400 μ sec at 50 Hz (100 watts average power) and operates at 780 - 815 nm. (37:73) While current limitations on output power appear to be limited only by the capability to cool the system, these large arrays have produced up to 300 W average output (34:195). For coherent detection, high-power MOPA devices have produced up to 700 mW of diffraction-limited CW power at 830 nm (7:328).

Optics

Currently in optics there are three general approaches to beam steering -- moving the entire telescope, moving a large flat mirror at the entrance pupil of the telescope (post objective beam steering), and moving a small mirror at the exit pupil of the telescope (pre-objective beam steering) (29:15). While each method is very effective for ground-based systems, they would prove difficult for a space-based surveillance system which requires both a large field-of-regard and ability to track large numbers of fast moving targets. The SDI program is faced with the same problems and have developed a system called the Portable Rapid Optical Beam Steering LADAR System.

The system uses a roving fovea with an oversized spherical primary mirror and aspheric secondary mirror as shown in Figure (4-1). The beam steering is accomplished by pivoting the secondary mirror about the primary mirror's center of curvature. Coudé mirrors in the secondary gimbal redirect the beam to a stationary external path. This system can provide diffraction-limited performance with a field-of-regard of 60° and beyond. The tested system provides a 3° step time of 18 milliseconds and a pointing jitter of less than 10 microradians (RMS). Using an angle sensing interferometer improved the pointing jitter to better than 1 microradian peak-to-peak (29:16).

The size of the entrance pupil to the optics will play an important role in the gain of the transmitter and receiver as well as the pointing and jitter requirements of the system. The beam divergence for a diffraction limited laser beam is approximately

$$d\Omega = \frac{4\lambda^2}{\pi D^2} \quad (4-1)$$

where D is the diameter of the beam or final collimating optical element (44:72). Since a smaller beam divergence results in a higher flux on target, it would appear that shorter wavelength systems with large entrance pupils would have a great advantage. But, to

operate near the maximum intensity of the far-field beam, the beam pointing accuracy must be smaller than the laser divergence angle. To maintain an illumination of ≥ 50 percent, the maximum pointing accuracy and jitter maintenance must be approximately $\pm 0.8 \lambda / D$ (44:73). Therefore, the maximum usable entrance pupil diameter as a function of wavelength is given by

$$\text{Maximum Entrance Pupil Diameter} = \frac{0.8\lambda}{\text{Jitter}} \quad (4-2)$$

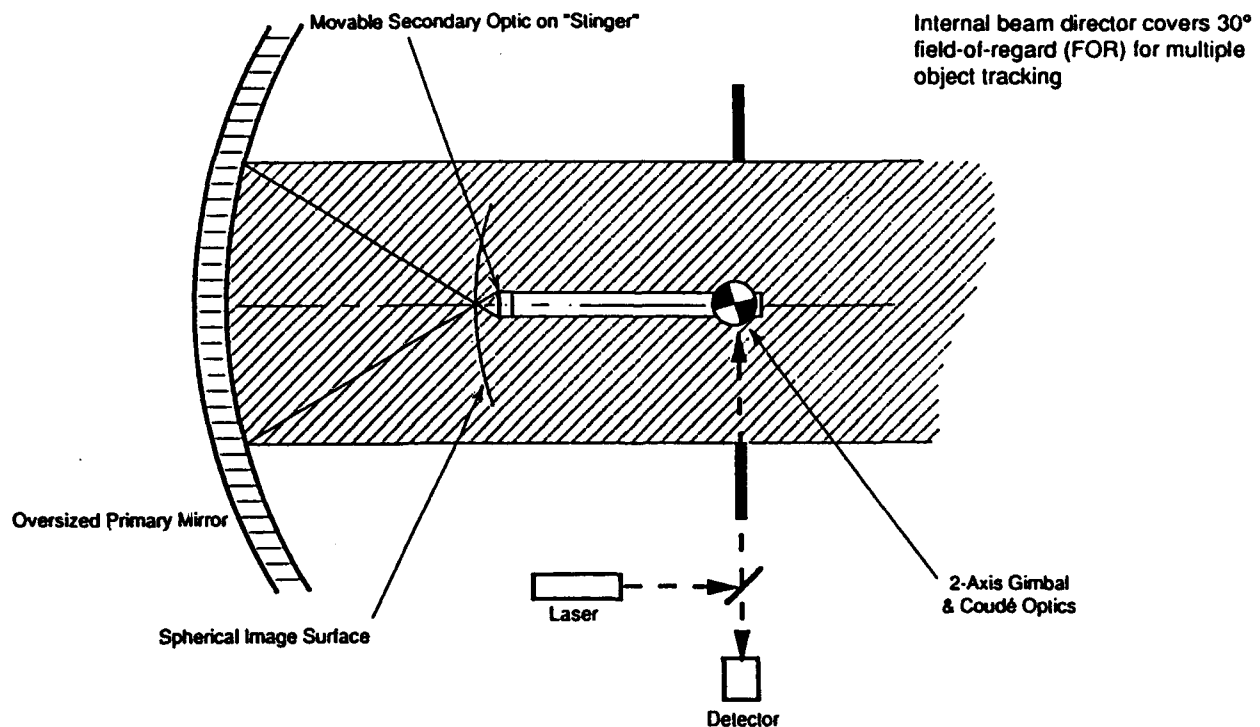


Figure 4.1 Schematic of Roving Fovea

Using a 1- μ radian jitter for the system, the maximum usable entrance pupil diameters for the various lasers under consideration are given in Table 4-2. Although the table indicates that a maximum diameter for the CO₂ laser system to be 8.48 m, this is currently unrealistic for a space system. For this thesis, a more acceptable value of 1.2 m will be used as the maximum diameter for the CO₂ system.

Table 4.1

Maximum Usable Entrance Pupil Diameter for Various Wavelengths as a Function of Achievable Beam Jitter

Wavelength	10.6 μ m	1.06 μ m	0.985 μ m	0.96 μ m	0.83 μ m	0.80 μ m
Maximum Entrance Pupil Diameter	8.48 m	0.848 m	0.788 m	0.768 m	0.664 m	0.64 m

From the definition of F-number on Page 3-27, it can be seen that by decreasing the focal length or increasing the diameter of the optics will result in a lower F-number. A shorter focal length increases the pixel FOV and, hence, provides more source area from which light can be collected. Larger diameter optics will allow more light to enter the system and result in a smaller diffraction-limited spot size. A small spot size is desirable for this type of detection system as it will limit the number of pixels over which the return energy is distributed. The difficulty with low F-number systems is that they are more difficult to construct (therefore more costly) and usually have increased aberrations. Figure 3.6 relates the direct detection efficiency to the Airy spot size and system F-number. For a wavelength of 0.7 μ m, an F-number of less than 8.9 should be used to provide high efficiency. For this thesis, a F-number of 2.2 is used as this system has already been developed and is in use. Using this F-number and an average wavelength of

0.7 μm , the diffraction-limited spot size is 1.88 μm which will contain approximately 84 percent of the total image energy.

Visible Detector

The visible sensor selected for this thesis is the 420 x 420 back-illuminated CCD focal plane array proposed for the Space-Based Visible (SBV) sensor discussed in Chapter 2. The CCD staring array provides a large instantaneous field-of-view, a high quantum efficiency and low read-noise. The pixels are 27 μm square and have less than 6 electrons rms equivalent noise when read out at 0.5 and 1.0 Mpixel/second (10:50). While initial instincts may indicate that SNR is maximized when the diffraction-limited spot size is matched to the detector size, previous analysis has shown that the larger pixel sizes increase the SNR due to increased integration time on target (22:45). Larger pixel sizes will decrease angular resolution and, for a set number of pixels, increase sensor FOV. For the systems selected, the angular resolution and FOV of the visible systems are given in Table 4-2.

Table 4.2

Angular Resolution and Sensor Field-of-View for Various Entrance Pupil Diameters

Entrance Pupil Diameter	1.2 m	0.848 m	0.788 m	0.768 m	0.664 m	0.64 m
Wavelength	10.6 μm	1.06 μm	0.985 μm	0.96 μm	0.83 μm	0.80 μm
Angular Resolution (in deg)	5.9×10^{-4}	8.3×10^{-4}	8.9×10^{-4}	9.2×10^{-4}	1.0×10^{-3}	1.1×10^{-3}
Sensor FOV (in deg)	0.25	0.35	0.37	0.38	0.44	0.46

The diffraction-limited spot from the target may not necessarily be contained within a single pixel. The pixel with the largest electrical current is the most important as it is the one which will determine if the detection threshold has been crossed. The expected energy from an image can be calculated from the geometry of the detectors and the statistical distribution of the signal. For ease of calculations, the outer rings of the Airy function are ignored resulting in only 84 percent of the incident power being received. This is a pessimistic assumption and, therefore, the actual expected energy should be greater than the one calculated in this paper. Since the diffraction-limited spot ($1.88 \mu\text{m}$) is smaller than the detector ($27 \mu\text{m}$), the energy of the image can be distributed into as many as 4 pixels (assuming no or very little gap between pixels). If the photon distribution within the image is assumed to be uniform vice an Airy function, then a methodology developed by G.J. Mayer may be used to calculate the expected maximum energy in a pixel (28).

Mayer's analysis is based on calculating the minimum of the maximum expected possible signals from a single pixel and can be expressed as (28:5)

$$E(s) = \sum_n S_n P_n \quad (4-3)$$

where

$E(s)$ = the expected maximum signal

S_n = the maximum signal possible from a single pixel within the group of n pixels containing all of the signal

P_n = the associated probability when all of the signal is contained in those n pixels

For a system where the signal can only be spread over no more than four pixels, the value of S_2 would be 0.5. This is explained by the fact that even though the signal may be at a

higher value than 0.5 if it occupies more than half the pixel, the 0.5 value is the lowest value that can be contained in one of the two pixels. In other words, this is the minimum amount of energy that can be located in the pixel that has received most of the signal. Adjusting for the Airy disk loss, the values of S_n for an image overlaying a maximum of four pixels are:

$$\begin{aligned} S_1 &= 1.0 \times .84 = .84 \\ S_2 &= 0.5 \times .84 = .42 \\ S_3 &= .87 \times .84 = .73 \\ S_4 &= .25 \times .84 = .21 \end{aligned}$$

The values for P_n (for $D < L$) are determined from the following formula's (28:13):

$$\begin{aligned} P_1 &= (L-D^2) / L^2 \\ P_2 &= 2D (L-D) / L^2 \\ P_3 &= D^2 (1-\pi/4) / L^2 \\ P_4 &= D^2 \pi / 4L^2 \end{aligned}$$

where

L = pixel diameter

D = spot diameter (first null of Airy function)

LADAR Detector

In order to facilitate the hand-off of the detected target from the visible sensor to the laser radar detector, the detector FOVs and, hence, their sizes should be approximately the same. For the purposes of this thesis, a laser radar detector size of 30 μm is assumed and all detectors are assumed to be cooled to 77 K to reduce thermal noise. The detector types to be used are:

CO_2 - HgCdTe quadrant detector

Nd:YAG - Silicon avalanche quadrant photodiode
Semiconductor lasers - Silicon avalanche quadrant photodiodes

The choice of detector materials provides the greatest efficiencies for the selected wavelengths. The avalanche photodiode was selected over the PIN photodiode due to its ability to provide gain. As seen from Equation (3-34), an increase in SNR will be achieved with an increase in gain as long as the thermal term is dominant. While the gain enhances the SNR for direct detection, it has no effect on coherent detection systems. In an optimized coherent system, the shot noise from the local oscillator is already the dominant noise source and any gain in signal is nullified by equal gain in noise. Therefore, either a PIN or avalanche photodiode will be used depending on which provides better efficiency and wider bandwidth.

Satellite Orbit

The determination of the orbit will affect not only the satellite sensor design and capabilities, but also the magnitude of the spectral reflection of the target. In order to maximize the target return energy for detection in the visible band, a sun-synchronous orbit is selected. In this orbit, the sensor can view objects near the earth shadow where they are the brightest. In addition, the satellite will be nearly always in sunlight and can, therefore, utilize solar panels instead of batteries which should provide for greater satellite lifetime and reduced thermal cycles. The major drawback of this type of orbit is the lower launch payload capability.

The satellite altitude affects the maximum range to target, orbital perturbations, and GPS accuracy. While an increase in altitude will provide a decrease in distance to some parts of the geosynchronous belt, it will also increase the distance to other parts of the belt. In order to reduce the maximum detection distance, a lower altitude orbit is

preferable. If the orbit is too low, the cross track field-of-regard of the sensor will be partially obscured by the earth. The lower orbit will also increase the orbital perturbation due to atmospheric drag. As this is the major orbital perturbation for low-earth orbits, minimizing its effect will increase satellite lifetime.

One additional factor considered in selecting the satellite altitude is that of GPS coverage. As stated in the thesis by Davey, one of the critical problems facing a space-based detection system is the ability of the system to provide updated orbital elements in an Earth-Centered Inertial (ECI) coordinate system. This requires that the satellites' ECI position be constantly updated. One of the most accurate and easiest methods to accomplish this task is through the use of a GPS receiver onboard the satellite. Although the use of GPS for satellite position determination is just starting to be investigated, it is considered to be quite possible. The main concern in determining the position accuracy is the same as that of an ground-based system and basically comes down to how many satellites are in view at any one time and the relative angles between the sensor and these satellites.

One of the prime figures of merit for GPS is the Position Dilution of Precision (PDOP). This parameter indicates the decrease in positional accuracy from that which would be obtained from a perfect geometric solution. For a PDOP of 4, the positional error is approximately 6 meters (40:68). Figures (4-2), (4-3), and (4-4) indicate the altitude at which PDOP is greater than 4 for 0° N, 30° N, and 60° N latitude. The graph is plotted from data received from Lt Col Thomas S. Kelso, Professor of Space Operations at the Air Force Institute of Technology, which represents a the 24 hour period on 1 November 1993.

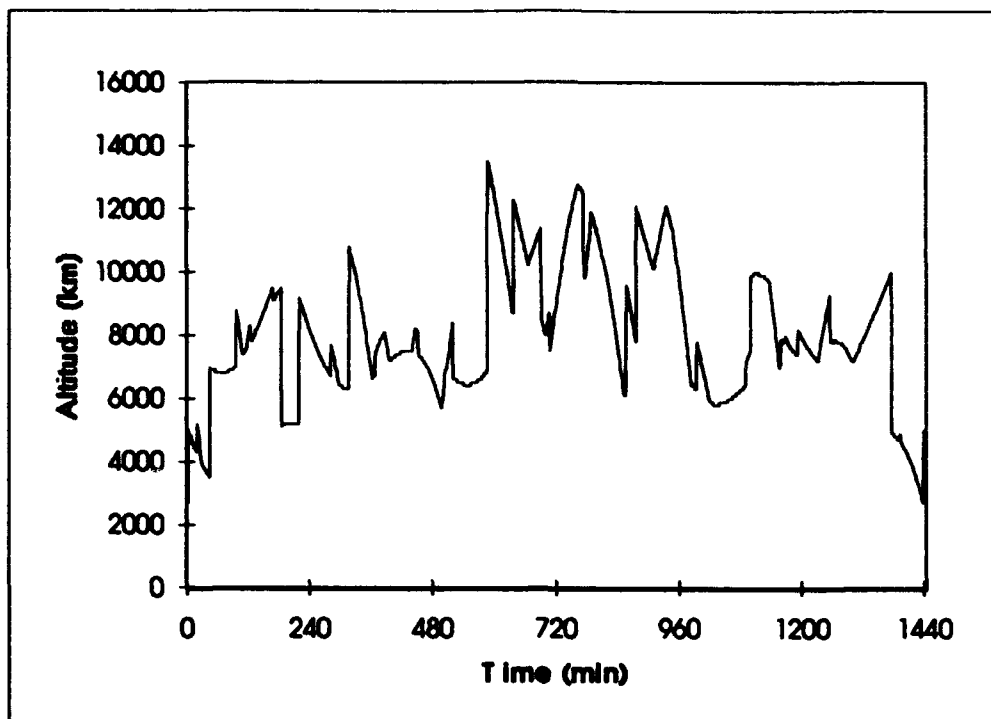


Figure 4.2 PDOP 4 altitude as a function of time for 0° N

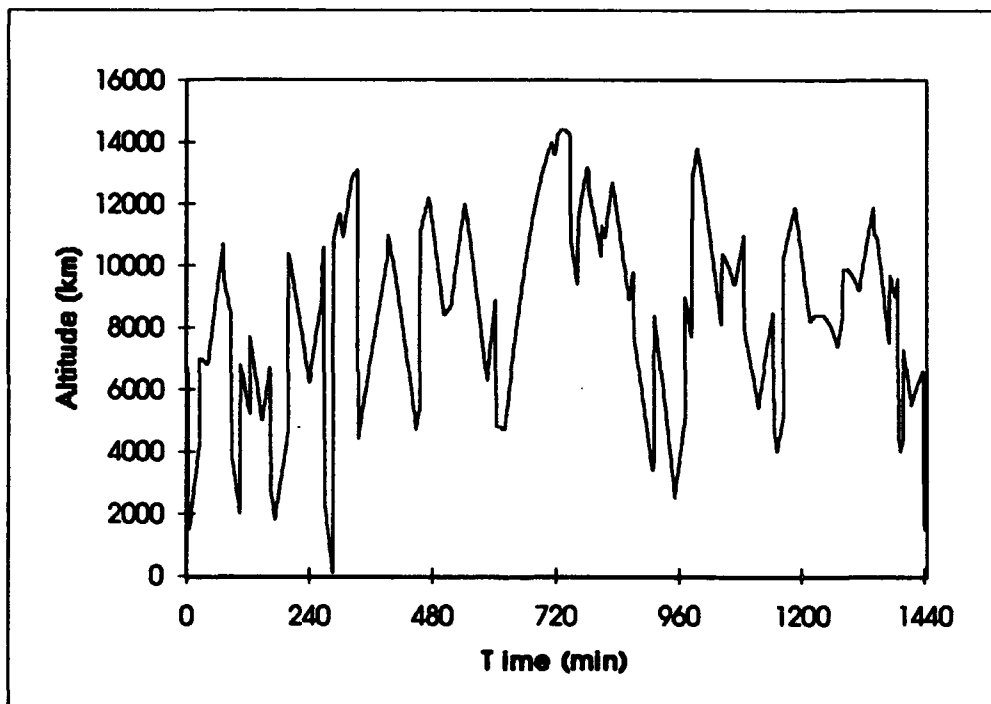


Figure 4.3 PDOP 4 altitude as a function time for 30° N

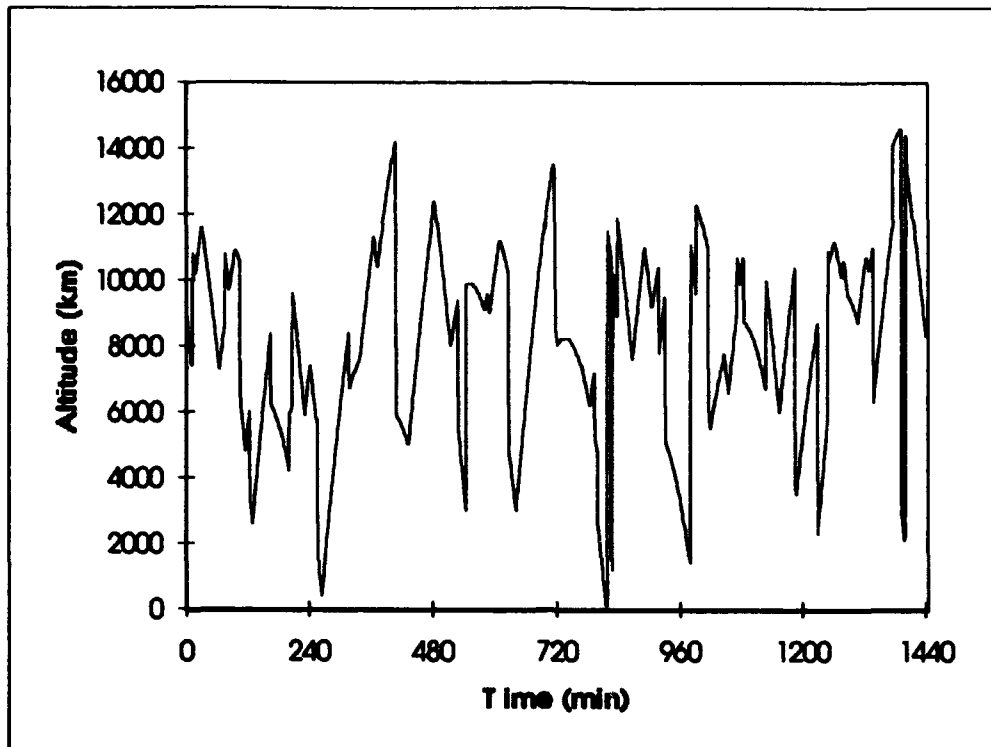


Figure 4.4 PDOP 4 altitude as a function of time for 60° N

The graphs show that as the latitude increases from the equator, the PDOP reaches a value of 4 at a lower altitude indicating a decrease in GPS accuracy. For the altitude of concern for this thesis (below 1,000 km), the PDOP is only worse than 4 for a few minutes a day. Although not plotted, the PDOP at the earth's surface during these time periods is just as bad if not worse. But even in the worst-case latitude, the PDOP is definitely able to provide sufficient accuracy below 1,000 km. Therefore, in order to provide good GPS accuracy and minimum atmospheric drag effects, an orbital altitude of 800 km is selected.

V. Design Selection and Performance Analysis

Introduction

The previous chapters have selected the system components and provided the necessary formulas in order to assess the relative performance capabilities of the proposed designs. This chapter will accomplish the design analysis in two major steps. The first step determines the received power from each proposed transmitter and selects the design which is most capable of detecting a selected target. The second step is to compare this proposed system's detection performance with that of GEODSS.

Transmitter Selection

In order to compare the proposed laser transmitters, a target scenario must be defined. To ease comparison and alleviate viewing angles, targets will be compared, for the visible system, using the product of target reflectivity and projected illumination area. For the laser transmitter, the product of laser cross section and projected illumination area will be used. This parameter will be initially set to 1 square meter for both cases. Previous research has shown that although lower orbit satellites have higher angular velocities, the increased range of geosynchronous satellites results in a lower SNR and, therefore, are more difficult to detect (22:43). In order to test the system against most difficult scenario, the target is assumed to be in geosynchronous orbit.

For the purposes of analysis, the constellation is considered to consist of two satellites with ascending node times differing by 12 hours, resulting in a maximum range to geosynchronous orbit of 42,980 km. While other orbits, such as Molniya, may exceed this range during their orbital period, it is assumed that target ranging will be scheduled such that the satellite is within the specified maximum range. Using a sun-synchronous altitude

of 800 km for the sensor satellite, the largest relative radial velocity between target and sensor is expected to be approximately 15 km/sec from the Molniya satellites.

In order to calculate the expected received power, using Equation (3-40) several additional system parameters must be defined. The transmitted power in that equation is the peak power of the system. The conversion between average and peak power for a pulsed laser system is

$$P_{avg} = P_{peak} \tau PRF \quad (5-1)$$

where

τ = the pulse width

PRF = the pulse repetition frequency

The pulse width of the CO₂ system discussed earlier was not defined in Dezenburg's article and is assumed to be 1 μ sec which is typical for these type of laser systems. The peak powers of the various lasers are defined in Table 5-1.

Table 5.1

Peak Power for Selected Transmitters

LASER TYPE	PEAK POWER	TYPE OF DETECTION
CO ₂	7 MW	Direct and Coherent
Nd:YAG	73 MW	Direct
Nd:YAG	44 MW	Coherent
InGaAs	360 W	Direct
InGaAs	1 W	Coherent
GaAlAs	5 kW	Direct
GaAlAs	700 mW	Coherent

The system efficiencies to be determined are optical transmission, obscuration ratio, and transmitter and receiver efficiencies. The optical transmission for this thesis is set to 0.99 which is probably slightly optimistic. The obscuration ratio is set to 0.1 which is the expected central obscuration for roving fovea design. From Figure 3-4, the on-axis transmitter efficiency (η_t) for an obscuration ratio of 0.1 is 0.786. The σ_d values (which relate detector radius to system F number) for the direct detection receiver efficiencies based on a pixel size of 30 μm are calculated using the relationship on Page 3-27 and shown in Table 5-2. In the case of the coherent detection receiver efficiency, the ratio of the detector radius to the Airy spot size (r) is used in place of σ_d since it is this value which is used to determine the efficiency. The detection efficiencies (η_d) for the various selected transmitters can then be determined using Figure 3-6 and Figure 3-9. These values are given in Table 5-3.

Table 5.2
Detection Efficiency Parameters for Selected Transmitters

LASER TYPE	σ_d VALUE	DETECTOR/AIRY RATIO (r)	TYPE OF DETECTION
CO ₂	2		Direct
CO ₂		0.53	Coherent
Nd:YAG	20		Direct
Nd:YAG		5.3	Coherent
InGaAs	22		Direct
InGaAs		5.7	Coherent
GaAlAs	27		Direct
GaAlAs		6.8	Coherent

The lower efficiency of the CO₂ system is due to the larger diffraction-limited spot size. In order to increase the receiver efficiency, a larger detector is required. For the direct detection receiver, a detector radius of 150 μm increases the σ_d value to 20 and,

hence, the detection efficiency is increased to 0.9654. For the coherent detection system, an increased detector radius of 42 μm increases the detector/Airy ratio to 0.7445 and, hence, the efficiency increases to 0.7837. In order to provide maximum efficiency for the system, these new detector sizes will be used for calculations involving the CO_2 laser transmitter. The overall receiver efficiency can then be calculated using Equation (3-44).

Table 5.3
Detection Efficiencies (η_d) for Selected Transmitters

LASER TYPE	DETECTION EFFICIENCIES	TYPE OF DETECTION
CO_2	0.6146	Direct
CO_2	0.6118	Coherent
Nd:YAG	0.9654	Direct
Nd:YAG	0.7775	Coherent
InGaAs	0.9669	Direct
InGaAs	0.7775	Coherent
GaAlAs	0.974	Direct
GaAlAs	0.7775	Coherent

The received power for the various transmitters are then calculated using Equation (3-40). These values are given in Table 5-4.

Table 5.4
Received Power for Selected Transmitters

LASER TYPE	RECEIVED POWER (Watts)	TYPE OF DETECTION
CO_2	1.38×10^{-15}	Direct
CO_2	1.12×10^{-15}	Coherent
Nd:YAG	3.6×10^{-13}	Direct
Nd:YAG	1.75×10^{-13}	Coherent
InGaAs	1.46×10^{-18}	Direct
InGaAs	3.43×10^{-21}	Coherent
GaAlAs	1.42×10^{-17}	Direct
GaAlAs	1.7×10^{-21}	Coherent

In order to calculate the signal-to-noise ratio (SNR) for each transmitter, the detector performance characteristics and system noise parameters must be determined. The signal portion of the SNR is determined by using the received power just calculated and Equation (3-6). Since the detector performance characteristics are unique to the wavelength being utilized, each system noise parameter must be calculated separately. In these calculations a narrow band filter of 50 nm is assumed for all receivers in order to reduce background noise.

CO₂ Laser Transmitter

The background radiance in the 10.6 μm band is $3.5 \times 10^{-11} \text{ W}/(\text{cm}^2 \text{ sr } \mu\text{m})$ (42:3-42). In order to convert this to a background radiance using Equation (3-9), the bandwidth and responsivity of the detector are required. The bandwidth of the direct detection system is simply $1/(2 \times \text{pulse width})$ while that of the coherent detection system is limited by the frequency shift of the doppler return signal. The doppler frequency is given by

$$f_d = \frac{2V_r}{\lambda} \quad (5-2)$$

where V_r is the relative radial velocity of the target (14:49). Using a relative velocity of 15 km/sec, the bandwidth required is $2.83 \times 10^9 \text{ Hz}$. This large bandwidth requires a detector with sub-nanosecond rise time which limits the selection to photovoltaic type of detectors. The typical responsivity of these type of detectors is 4.3 A/W. The smaller bandwidth of the direct detection system permits the use of a photoconductive detector with a typical responsivity of 30 A/W and a detectivity of $5 \times 10^{10} (\text{cm-Hz}^{1/2}/\text{W})$ (14:136). The noise current is calculated using the relationship between D^* and noise

power given in the definition of terms of Equation (3-34). Applying these values to Equation (3-3) yields the power SNR for the two systems which are given in Table 5-5.

The coherent system SNR is limited mainly by the bandwidth required due to the doppler shift while the direct detection system is limited by the relatively large detector noise caused mainly by dark current (assuming detector cooled to 77K). While the coherent system provides a higher SNR than the direct detection system, neither is high enough to support detection of a satellite at the proposed range.

Nd:YAG Laser Transmitter

The background irradiance for the near IR and visible transmitters are calculated using only zodiacal light as a background source and, therefore, it is assumed that tracking is not attempted when either the sun or moon are in the FOV of the sensor. The brightness of the zodiacal light is 13 M_v (visual magnitude) per square arc-minute (22:20). Visual magnitude is converted to satellite irradiance by (33)

$$E_{sat}(\lambda) = E_{sun}(\lambda) (1.944 \times 10^{-11}) (10^{-0.4(M_v)}) \text{ (W/m}^2 \text{ } \mu\text{m)} \quad (5-3)$$

Both an APD and a PIN diode detector were used to determine the SNR of the direct detection system in order to compare performances. The APD was EG&G Optoelectronics C30902S at -25 °C . The PIN diode performance was based of performances of EG&G Optoelectronics SGD-040A and YAG 444-4 detectors (11). The APD resulted in a higher SNR and, therefore, only the APD results are included in Table 5-5. The SNR is dark-noise limited in the direct detection case with a dark current of 0.2 nA. In the coherent detection case, the SNR is bandwidth limited. While the performance of the Nd:YAG system is slightly better than that of the CO₂ system, the SNR is still not large enough to allow detection from low-earth orbit.

InGaAs Laser Transmitter

The detector selected for the InGaAs was the EG&G Optoelectronics C30902S at -25 °C. This results in a dark current of 0.2 nA which limits the detection capability of the direct detection system. The pulse width was set to 3.3×10^{-6} sec to provide an arbitrarily set range resolution of 500 meters. The SNRs for the coherent and direct detection techniques are far below those of the CO₂ and Nd:YAG systems.

GaAlAs Laser Transmitter

The same APD detector used for the InGaAs is used for the GaAlAs. The SNRs for the GaAlAs are much higher than the InGaAs due to increased detector efficiency at the shorter wavelength but are still far below those required for detection of the satellite. The main reason for the poor performance is the low peak powers available with semiconductor laser systems.

Table 5.5

Received Signal-to-Noise Ratios

LASER TYPE	SIGNAL-TO-NOISE RATIO (POWER)	TYPE OF DETECTION
CO ₂	4.14×10^{-14}	Direct
CO ₂	1.06×10^{-5}	Coherent
Nd:YAG	1.6×10^{-7}	Direct
Nd:YAG	1.9×10^{-5}	Coherent
InGaAs	1.1×10^{-14}	Direct
InGaAs	1.5×10^{-13}	Coherent
GaAlAs	5.4×10^{-12}	Direct
GaAlAs	1.5×10^{-13}	Coherent

Alternate Transmitters

Obviously, none of the SNRs are sufficient enough to allow for detection. Since the limiting factor for all the coherent detection techniques is the bandwidth required in order to detect the doppler shift, the only way to increase the SNR is to increase the

received power. It is highly unlikely the required SNR can be achieved without a moderate increase in satellite altitude. Since it is preferable to maintain the lower altitude for both use of the GPS system as well as to decrease the number of satellites required for complete coverage, other means of increasing SNR were investigated.

The limiting factor in the direct detection transmitters was the dark current in the system. Although this can be reduced through the use of smaller detectors or narrow bandwidths, it can not be reduced sufficiently to allow for detection. One method of eliminating the limiting factor of dark current is to switch to a CCD detector. Employing the same type of detector as was described earlier for the visible detection allows the system noise to be limited to the read noise of the detector and the shot noise of the signal. The signal-to-noise ratio for the CCD detector can then be written as

$$SNR = \frac{\overline{N_s}^2}{\overline{N_s} + \sigma_m^2} \quad (5-4)$$

where

- $\overline{N_s}$ = the average number of photoelectrons generated due to received signal pulse and is given by Equation (3-1) where T is the pulse width
- σ_m^2 = the detector read noise (6 electrons per pixel)

For the purposes of analysis, a pixel size of 15 μm in diameter is selected and placed in a 4x4 CCD matrix which can be signal processed to act like a quad receiver, if desired. Due to the small integration times (3.3 μsec for 500 meter range resolution) the number of pixels is intentionally kept low in order to maintain the read out rate at about 1 MHz. Reading four pixels every 6.6 μsec results in a read out rate of 600 kHz. One minor problem is the requirement to read out the information while maintaining constant range coverage. This can be overcome by using two separate CCD detectors and

employing some method of switching between the two arrays at the end of each range gate.

The spectral efficiency of the CCD detector does not allow for good detection in the IR which eliminates the possible use of the CO₂ laser transmitter. The Nd:YAG though can be frequency doubled to produce output at 530 nm with an output power of approximately 40 percent of the original transmitter power. Using Equation (4-2), the maximum optical diameter due to jitter for the frequency doubled Nd:YAG system is 0.424 meters.

The jitter restricted size of the entrance pupil will ensure that the minimum power received by the target will be 50 percent of the transmitted power. Therefore, the following calculations will use two scenarios. The best-case scenario assumes the target receives the maximum transmitted power. The worst case assumes the target only receives 50 percent of the transmitted power. Using Equation (4-3), the expected maximum signal return in any pixel is 0.76. The results of using the CCD detector are given in Table 5-6.

Table 5.6
CCD Detector Signal-to-Noise Ratios

LASER TYPE	SNR (POWER) (BEST CASE)	SNR (POWER) (WORST CASE)
Nd:YAG	0.2014	5.5×10^{-2}
InGaAs	1.4×10^{-6}	3.4×10^{-7}
GaAlAs	1.6×10^{-3}	4.1×10^{-4}

In order to determine if these values are sufficient for detection, the required probability of false alarm (p_{fa}) must be determined. The use of equation (3-39) requires that the p_{fa} , the time between false alarms, the number of pulses to be integrated and the

time that no gates are opened be specified or determined. Since the range is determined by a single pulse and the range rate by the change in range over several pulses, a time between false alarms of 10 seconds should be sufficient to provide required accuracy. The range gate on-time for a 500 meter resolution is 3.3 μ sec. Setting the overall range distance to be searched to 500 km results in 1,000 range gates and a required p_{fa} of 3.3×10^{-7} .

To determine the required SNR to achieve this p_{fa} , modifications would be required to Equations (3-21) and (3-23). The reason for the modifications is that the noise from the CCD is not modeled by Poisson statistics but follows zero-mean Gaussian statistics. This means that Equation (3-21) would be calculated using a Gaussian probability density function. Equation (3-23) though would be the convolution of the two pdfs since the signal still obeys Poisson statistics. I could not find this representative pdf during my research. Therefore, this thesis uses Poisson statistics for both signal and noise. The required SNR resulting from this assumption will be greater than that actually required and therefore the system should perform slightly better than predicted in this research.

The average number of noise photoelectrons per counting interval is set to 6 since the background noise is much less than the read noise of the CCD. Using this value and Equation (3-24), a threshold photoelectron count is determined for several probability of false alarms (p_{fas}). Using Equation (3-25), the number of noise and signal photoelectrons can then be calculated and hence the required SNR can be determined. The results of these equations using a probability of detection of 0.95 is plotted in Figure 5-1. The results indicate that a p_{fa} of 3.3×10^{-7} requires SNR of approximately 370. This SNR is much greater than that currently provided by the proposed system. In fact, applying the power of the signal received to Equation (3-40) and solving for range results in a best-case range

of 10,000 km and a worst-case range of 8,600 km for the transmitter with the highest power (Nd:YAG).

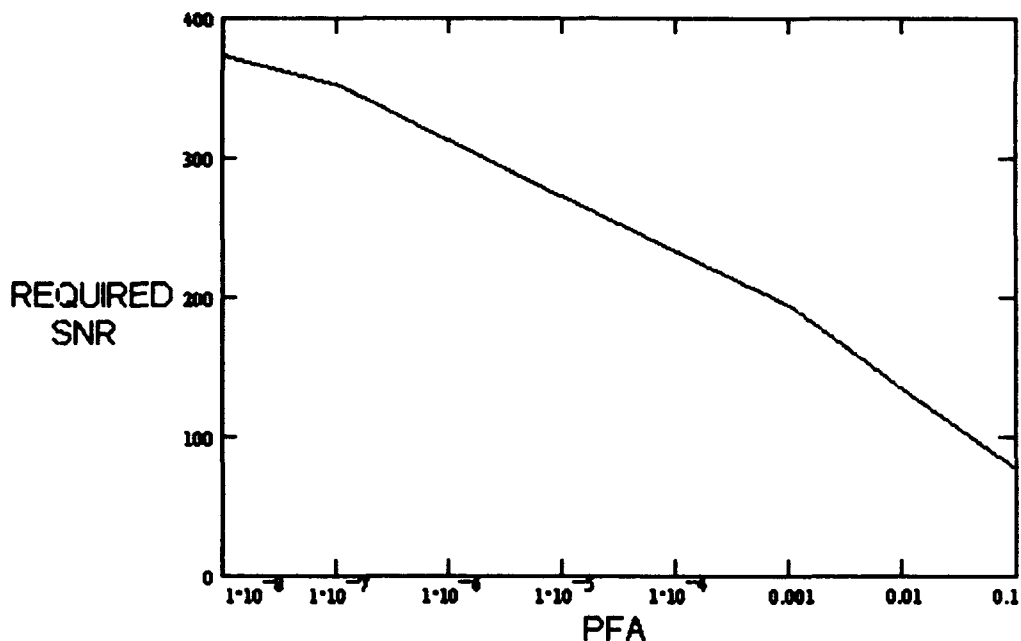


Figure 5.1 Required SNR as a function of probability of false alarm

One method to increase the SNR of the proposed system, and, hence, increase the detection range, is to decrease the range resolution of the system. This will increase the system integration time and allow for the use of pulse integration. Before analysis can be accomplished, several assumptions must be made and detection parameters determined. First, it is assumed that no other target is present in the field-of-view of the sensor during the integration period. This allows the calculations to assume all pulse returns are from the target. The unambiguous range to a target is defined as

$$R_{unamb} = \frac{c}{2 prf} \quad (5-5)$$

The unambiguous range for 40 and 50 pulses/sec is 3,750 and 3,000 km, respectively. This range limits the maximum size of the range resolution cell. The range resolution is defined as

$$R_{\text{res}} = \frac{ct}{2} \quad (5-6)$$

where t is the integration time/range cell.

The second assumption is that the detector is somehow blocked from receiving background noise when signal pulses are not being integrated in order to maintain the read noise as the dominant noise in the system. This may require a cooled moving device placed in the optical path or some method of beam steering. Additionally, since the round trip time for a single pulse to maximum range is 0.29 seconds, some type of pulse integration scheme must be assumed in order to allow for the transmission and receiving of pulses to occur without interference. For a 40- and 50-prf system, the maximum number of pulses that can be transmitted prior to the arrival of the first pulse (assuming maximum range) is 11 and 15, respectively. Therefore, this analysis assumes that after transmitting the maximum number of pulses, a receiving time of 0.3 seconds will occur before further transmission. The final parameter to be selected is the time between false alarms (tbfa). It is assumed that a false alarm for every 10 range measurements is acceptable. This results in an increasing tbfa as the integration time increases.

Figure 5-2 shows the detection range as a function of range resolution for the Nd:YAG transmitter. As shown, even in the best case scenario (maximum power on target), a range resolution of 1,000 km is still not sufficient to provide detection at the required maximum range. Figure 5-3 shows the range resolution for the GaAlAs laser

transmitter. The graph indicates that detection can occur if the range resolution for the best case is 48 km and 200 for the worst case.

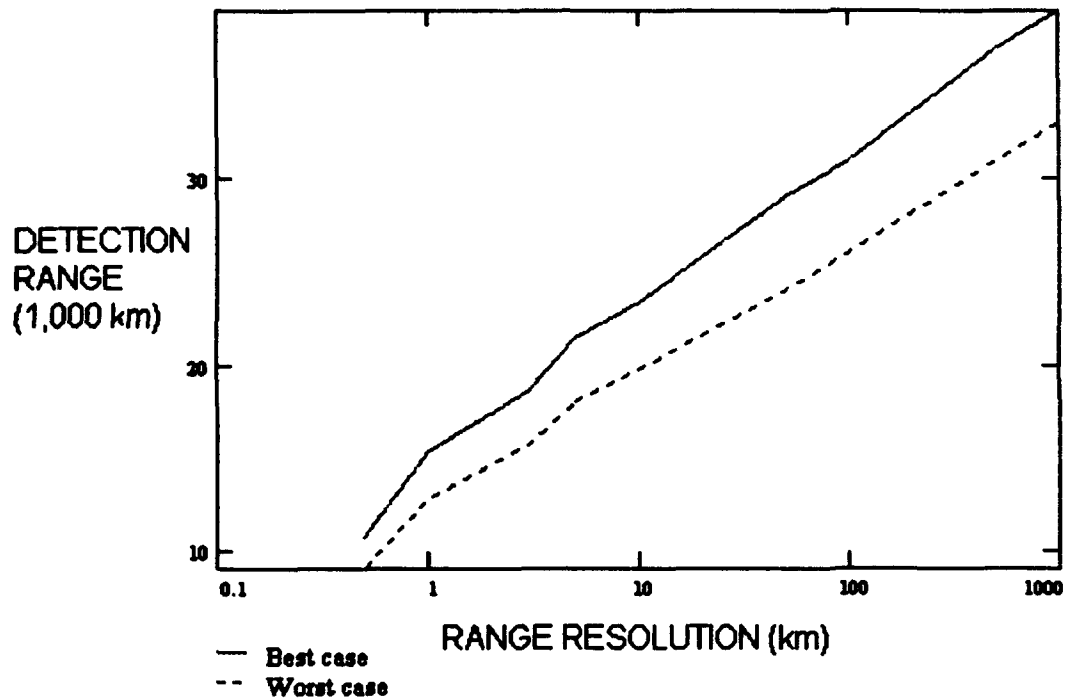


Figure 5.2 Detection range as a function of range resolution for Nd:YAG

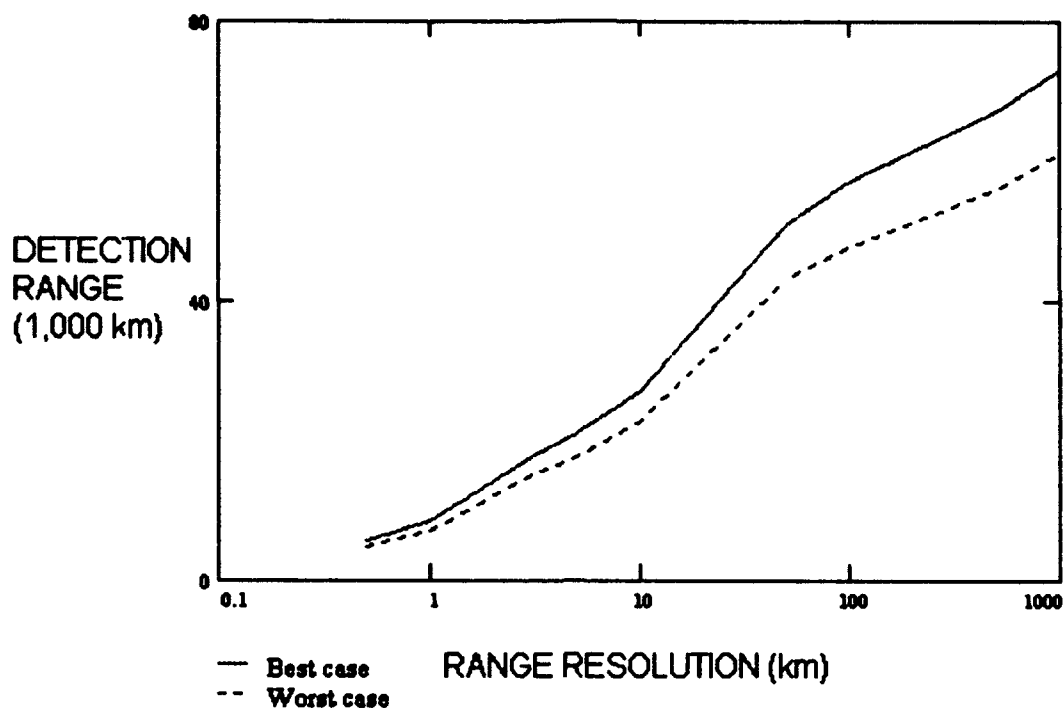


Figure 5.3 Detection range as a function of range resolution for GaAIAs

While Figures 5-2 and 5-3 are based on a target area of 1 m^2 , it is likely that the reflectivity/projected area product will be greater than this number for most satellites. Figure 5-4 shows the range resolution capability from the selected sensor sun-synchronous orbit as a function of target size. This graph is for the GaAIAs laser transmitter as it is the most promising.

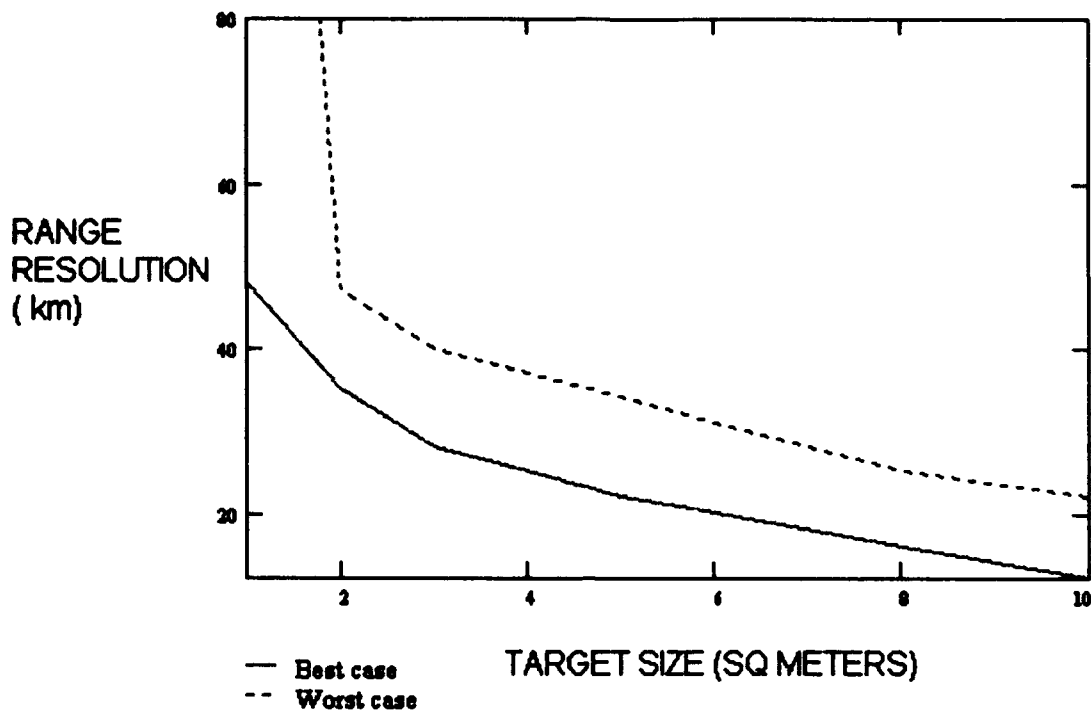


Figure 5.4 Range resolution as a function of target area for GaAlAs

Detection Capabilities of Proposed and GEODSS Systems

This section compares the visible detection performance of the frequency doubled Nd:YAG laser system with that of GEODSS. The Nd:YAG system was chosen since it has the smallest entrance pupil diameter and hence most stringent performance capability. The comparison is based on the optimum performance of GEODSS. A clear line of site is assumed to the target from the sensor zenith such that the irradiance from the target has to travel through a minimum of the earth's atmosphere. For the purposes of analysis, a site elevation for GEODSS of 4,000 ft is selected and the site is assumed to be in total darkness (no scattered sunlight or moonlight in FOV). The sensor is assumed to be in low-earth orbit for the comparison.

Proposed System Detection Capabilities.

In order to detect the targets, a detection scheme similar to GEODSS is assumed. The sensor is inertially fixed to a point in space such that the background can be eliminated and the target will appear as a streak. The limiting factor for maximizing the SNR is the amount of time a the target remains in a pixel field-of-view. The average angular rate of geosynchronous targets as viewed from sun-synchronous orbits is 36 arcsec/sec with a maximum relative angular rate of 50 arcsec/sec (22:22)(22:43). This results in an average dwell time (average case) of 0.092 seconds and a minimum (worst case) dwell time of 0.066 seconds.

Setting the bandwidth to $1/(2 \times \text{dwell time})$ and the optical transmission to 0.99 results in a system which has a shot noise approximately 10 times that of the read noise. The average number of background photoelectrons in the time interval of interest are 8.8 in the average case and 8.4 in the worst case. The expected maximum signal per pixel using Equation (4-3) is 0.782. The σ_d value for 15 μm pixel size is 15.3 which, from Figure 3-6, results in a direct detection efficiency of 0.952. These values are used to determine the power of the signal incident on the detector. The SNRs can then be calculated using Equations (3-3) and (3-6). The average and worst case SNRs for several target illuminated areas up to 0.4 m^2 are given in Figure 5-5.

GEODSS Detection Capabilities.

For targets in geosynchronous orbit, the relative angular velocity to a GEODSS site is 15 arcsec/sec (22:56). The maximum integration time is then 0.8064 seconds based on a 2.1 degree field-of-view and 625 pixels in that FOV. The transmission of the atmosphere is 0.91 for 4,000 km (41:14). The obscuration ratio for GEODSS is 0.643 giving a clear aperture area of 0.46 m^2 (22:58). The σ_d value for a 63- μm pixel size is 65.8 which, from the formula used to determine Figure 3-6, results in a direct detection

efficiency of 0.9741. Applying Equation (4-3), the expected maximum signal in a pixel is 0.82. For a gain of 2,000, the result is a system that is dark-noise limited for small target sizes. Although some literature states that GEODSS increases its gain in order to become shot-noise limited, this analysis indicates that for small targets GEODSS will require a significant increase in gain to overcome the dark current noise (22:54).

Figure 5-5 allows for comparison of the proposed Nd:YAG sensor average- and worst-case SNRs and that of GEODSS for various target areas. Even with the increased range and smaller optics of the Nd:YAG system, this proposed sensor provides an increased SNR when compared to GEODSS for targets below 0.225 m². After this point, the gain of the GEODSS system provides a higher SNR for targets above 0.35 m². This does not mean that any one system performs better than the other for automatic detection. In order to compare detection capability, the probability of false alarm must be determined and the SNR required to achieve that probability calculated. Figure 5-6 plots the required probability of false alarm for both systems as a function of the time between false alarms (tbfa). The longer integration time of the GEODSS sensor allows it to have a lower required p_{fa} to achieve the same tbfa.

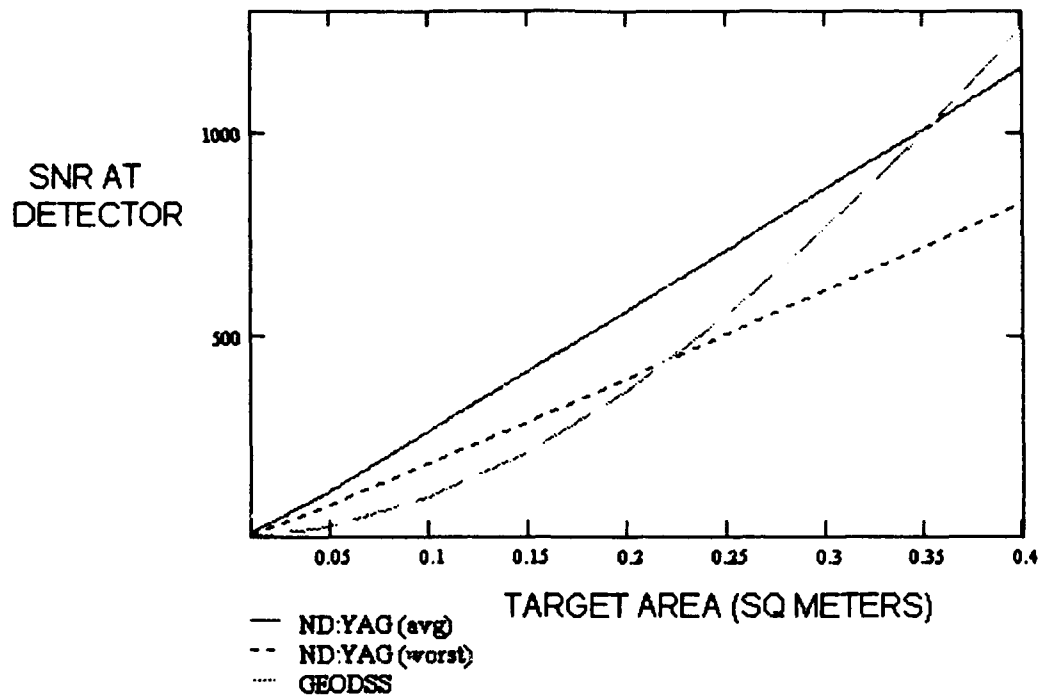


Figure 5.5 Proposed sensor and GEODSS SNRs as a function of target area

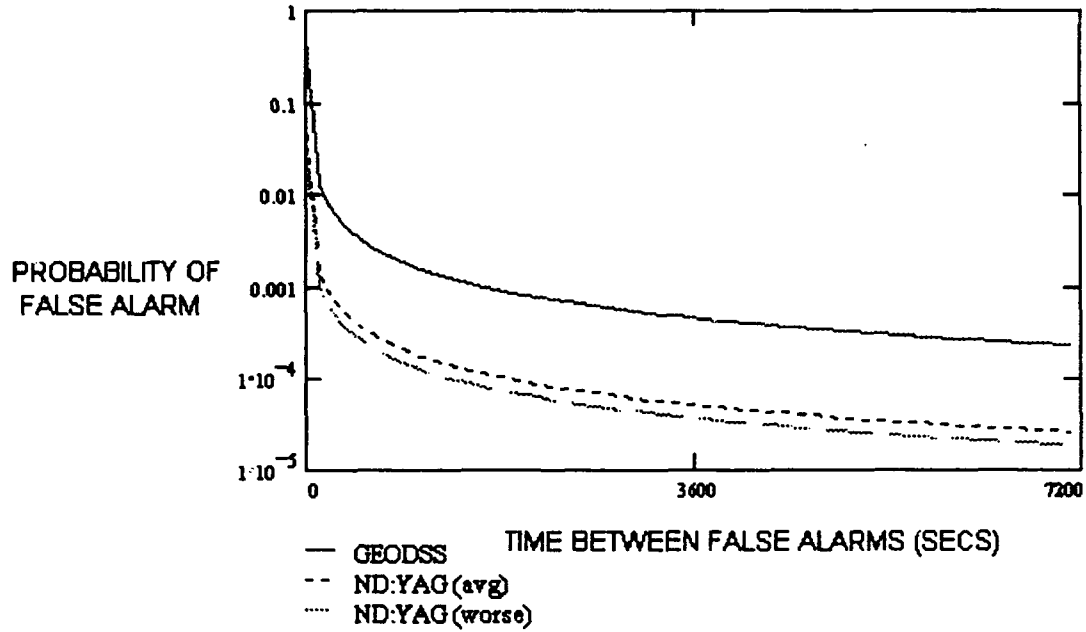


Figure 5.6 Probability of false alarm as a function of time between false alarms

Figure 5-7 compares the probability of false alarm as a function of the required SNR to achieve detection for the average- and worst-case target scenarios of the Nd:YAG system and the best- and worst-case detection capability of the GEODSS system. As shown, there is very little difference between the worst- and best-case target scenario of the Nd:YAG system. GEODSS has a very large difference between its best- and worst-case detection capabilities. In the best-case, the sensor is shot-noise limited and performs like a heterodyne receiver. In the worst-case, the system is dark-noise limited. Due to the large average number of photoelectrons per counting interval, the required threshold for detection, and, hence, the required SNR is quite high for a given p_{fa} .

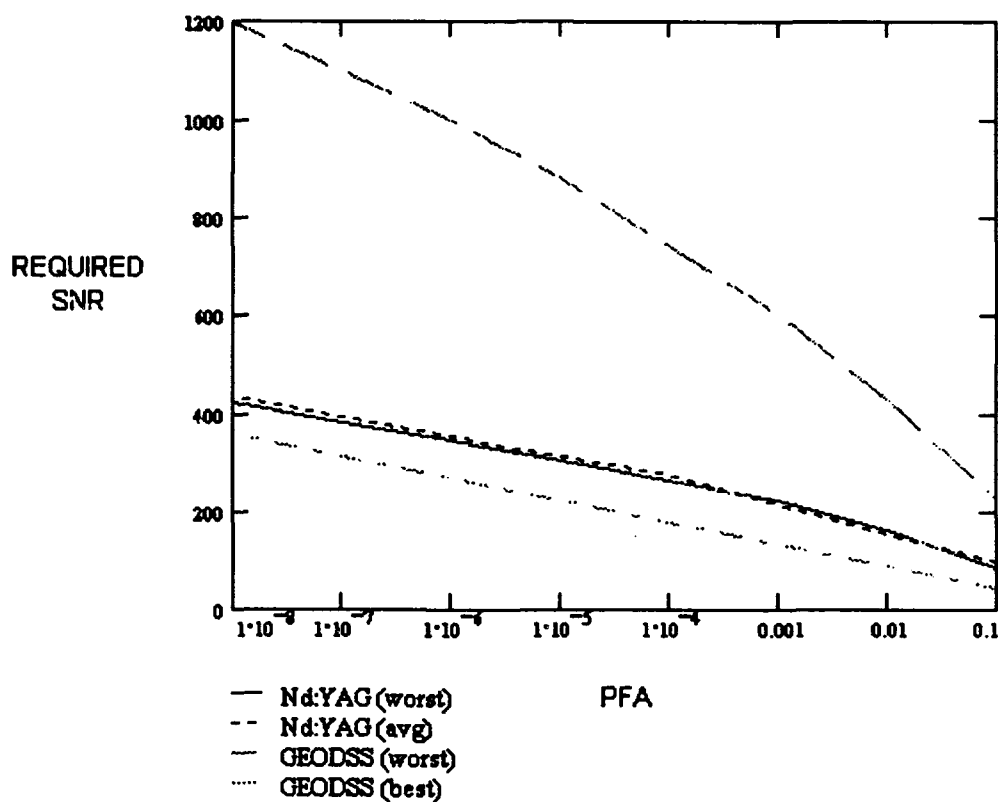


Figure 5.7 Required signal-to-noise ratio as a function of probability of false alarm.

To compare the target size detection capability of the two systems a time between false alarms of 1,800 seconds (30 minutes) is selected. From Figure 5-6, for a detection probability of 0.95, the required p_{fa} for the GEODSS system is 0.001 and 0.0001 for both cases of the Nd:YAG system. From Figure 5-7, the required SNR for the GEODSS system is approximately 600 for the worst case and 170 for the best case. The Nd:YAG best and worst cases are equal at 300. From Figure 5-5, the smallest size target capable of detection by the GEODSS worst case is 0.26 m^2 and is improved to 0.12 m^2 if the system is shot noise limited. In the case of the proposed Nd:YAG system, the target can be as small as 0.11 m^2 for the average angular rate target and 0.15 m^2 for the worst angular rate target. Therefore in this scenario, this proposed system is capable of automatic detection of most objects of smaller reflected size than that of the GEODSS system even if shot-noise limited. For targets of high angular velocity (worst case), the detection capability of the proposed system for the parameters chosen is better than GEODSS if GEODSS is dark-current-noise limited, and has only a slightly worse detection capability if GEODSS is shot-noise limited.

VI. Conclusions and Recommendations

Conclusions

The purpose of this research is to determine the performance requirements of a combined optical/LADAR space-based system in order to detect and track deep-space satellites from a near-earth orbit. The near-earth orbit is selected in order to provide for the use of GPS receivers to determine satellite ECI position as well as to reduce the number of satellites required to provide total coverage of all deep-space objects. A geosynchronous target is selected in order to maximize target range as this is expected to make it the most difficult scenario in order to detect the target. A sun-synchronous orbit is selected for the sensor satellite in order to provide maximum reflected detection area for the visible portion of the sensor. Assuming a minimum sensor constellation of 2 satellites, the maximum range to the target is 42,980 km.

After reviewing previous research in this area, this thesis developed the required expressions for power signal-to-noise ratios for direct and coherent detection. The relationship between these SNR values and the probability of detection, probability of false alarm, and time between false alarms are also determined in order that minimum signal-to-noise ratios may be determined from assumed user specifications. This research develops the necessary formula's in order to determine the power of the signal return from the target. The analysis of the return power includes optical transmission, transceiver obscuration, pixel geometry, and transmitter and receiver efficiencies.

Design components of the system are broken in three main areas: laser transmitter, optics, and detectors. Selection of the candidate LADAR transmitters were based on those currently be assessed for space-based laser communications and remote sensing and consist of the CO₂, Nd:YAG, InGaAs and GaAlAs lasers. The maximum output of these lasers is determined from current space-based designs or specifications. The transmitted

powers are selected for both a pulsed multi-mode (direct detection) and pulsed-single mode continuous wave (coherent detection) operation. The optics selected use a roving fovea design which uses a pre-objective beam steering technique to track the target. The size of the primary optic is limited by the 1 μ radian jitter of the system and is wavelength dependent. The optical diameters varied from 0.64 m for the direct detection GaAlAs transmitter to a self-imposed 1.2 m for the CO₂ system. The detector selection was based on efficiency of the detector at the transmitted wavelength. Initial selection included a HgCdTe detector for the CO₂ system, and avalanche photodiodes for the remainder of the transmitters.

Using a 15 km/sec worst case radial velocity from a Molniya orbit resulted in a doppler frequency bandwidth requirement ranging from 2.83×10^9 Hz for the CO₂ coherent transmitter to 3.61×10^{10} Hz for the coherent GaAlAs transmitter. Due to the dependent nature of the coherent SNR on bandwidth, the resulting SNR for all coherent systems is bandwidth limited and well short of the required value. In the case of the direct detectors, the power of the return signal is not strong enough to overcome the detector noise current. These limiting factors forced the consideration of using a CCD detector in order to reduce the noise.

The CCD detector could not be used to provide an output to an envelope detector of the IF frequency from the coherent lasers because this type of detector device stores the energy rather than providing an immediate read-out. While the CO₂ and 1.06 μ m Nd:YAG are not considered because they operate outside the responsivity of this detector, the frequency doubled Nd:YAG laser is considered due to its 530 nm wavelength and a power output of 40 percent of the original transmit power is assumed. The direct detection semiconductor laser transmitters are also considered as candidate systems using the CCD detector.

The use of the 530 nm Nd:YAG system imparted a limitation on the optical diameter of the system to 0.424 meters due to the 1 μ radian jitter of the roving fovea design. The Nd:YAG and GaAlAs systems were examined for both maximum transmitted power on target (best case) and 50 percent power on target (worst case). Using a single pulse return, a range resolution of 500 m, and a time between false alarms (tbfa) of 3 seconds resulted in a best-case detection range of 10,700 km and a worst-case detection range of 9,000 km for a 1-m² target area (reflectivity x projected area) with the Nd:YAG laser transmitter. For the GaAlAs, the best- and worst-case single-pulse detection ranges were 5,800 km and 4,900 km.

The only method examined that achieved sufficient SNR for detection was to decrease the range resolution in order to provide a longer integration time and allow for pulse integration. This allowed the longer pulse width of the GaAlAs to provide a higher average power on the target. This, combined with a larger entrance pupil diameter, resulted in a smaller required range resolution for the selected detection range. The capability of the proposed system to provide range and range rate information is highly dependent on the target size. For a 5-m² target, the system can provide a worst-case (50 percent power illumination) range resolution of 34 km from the low-earth sun-synchronous orbit.

The detection performance of the smallest entrance pupil proposed system was compared to GEODSS to determine its capability given a laser with sufficient transmitting power can be found in the future. An average (average case) and maximum (worst case) angular velocity were considered for the proposed satellite system. The dark-noise limited (worst case) and shot-noise limited (best case) scenarios were considered for GEODSS. With an arbitrary choice of time between false alarms of 30 minutes, the results indicated that the average case proposed system outperformed GEODSS's best-case scenario and was capable of detecting targets to a 0.11 m² (area defined as product of reflectivity and

projected illuminated target surface area) and worst-case detection to 0.15 m^2 . In the case of GEODSS, the best-case scenario was capable of detecting targets of 0.12 m^2 with a worst-case detection capability to 0.26 m^2 .

Recommendations for Further Study

There are several areas that have not been included in this study that warrant more detailed investigation. These include:

1. Determination of user accuracy requirements for velocity and range in order to provide orbital element updates. This will drive the time between false alarms and impact on the size of target that can be detected.
2. For a given set of user requirements, determine the number of sensor satellites and their best orbits in order to provide a user-defined update time on target satellites. From this point, a complete cost and performance comparison of the GEODSS system to a space-based satellite system can be accomplished.
3. Determine the capability of the proposed satellite system to support detection and tracking of low-earth-orbiting satellites which could possibly further reduce the number of required ground-based sensors.
4. Determine the ECI position accuracy required by the sensor and the capability of GPS to provide this accuracy. This would include the degradation of the GDOP with altitude which could limit the maximum altitude this system can be deployed to.

Bibliography

1. 1013 Combat Crew Training Squadron. *Space Operations Orientation Course Handbook, Second Edition*. Peterson AFB CO: Air Force Space Command, 1 January 1991.
2. Air University press. *Space Handbook*. AU-18, Maxwell AFB AL: Air University, January 1985.
3. Bachman, C. G. *Laser Radar Systems and Techniques*. Artech House Inc, Dedham, MA, 1979.
4. Beatty, J. Kelly. "The GEODSS Difference," *Sky & Telescope*, May 1982, pp. 469-473.
5. Boyd, R. W. *Radiometry and the Detection of Optical Radiation*. John Wiley and Sons, New York, 1983.
6. Canadian Forces School of Aerospace Studies. *Electro-Optics Manual*. CFB Winnipeg, Man, Canada, Jan 1990.
7. Cornell, Donald "High Power Master Oscillator Power Amplifier (MOPA) AlGaAs laser for intersatellite communications," *SPIE Free-Space Laser Communication Technologies IV 1635*: 328-336 (1992).
8. Davey, Flt Lt K. F. G. *Ground-Based Deep-Space LADAR for Satellite Detection: A Parametric Study*. MS thesis, AFIT/GSO/ENS-ENP/89 D-1. School of Engineering, Air Force Institute of Technology (AU), Wright-Patterson AFB OH, December 1989.
9. Dezenberg, George "SDI LADAR technology program update," *SPIE Laser Radar VII, 1633*: 2-5 (1992).
10. Dyjak, C. P. and D. C. Harrison. "Space-Based Visible Surveillance Experiment," *Surveillance Technologies*, edited by Sankaran Gowrinathan, Raymond J. Mataloni, Sr., and Stanley J. Schwartz. Proc. SPIE 1479: 42-56 (1991).
11. EG&G Optoelectronics. Product catalog. Montgomeryville, PA, no date (1993).
12. Hecht, Eugene. *Optics*. Second Edition, Addison-Wesley publishing Company, Reading, MA, 1990.

13. Howell, Captain J. Andreas, *The Challenge of Space Surveillance*. Sky & Telescope, June 1987, pp. 584-588.
14. Jelalian A. V. *Laser Radar Systems*. Artech House, Norwood, MA, 1992.
15. Joe, Edmond and Chang, John "Space-qualified three color solid state lidar," *SPIE Laser Radar VII: Advanced Technology for Applications 1633*: 33-40 (1992).
16. Johann, U. and Seelert, W. "1 W CW Diode-Pumped Nd:YAG Laser for Coherent Space Communication System," *SPIE Optical Space Communication II, 1522*: 158-168 (1991).
17. Katzman, M. *Laser Satellite Communications*. Prentice-Hall, Inc., Englewood Cliffs, NJ, 1987.
18. Kingston, R. H. *Detection of Optical and Infrared Radiation*. Springer-Verlag, Germany, 1978.
19. Klein, B. J. and Degnan, J. J. "Optical Antenna Gain. 1: Transmitting Antennas," *Applied Optics*, 13: 2134-2141 (September 1974).
20. Klein, B. J. and Degnan, J. J. "Optical Antenna Gain. 2: Receiving Antennas," *Applied Optics*, 13: 2397-2401 (October 1974).
21. Koechner, Walter, Richard Burnham, Jeff Kasinski, Pat Bournes, Don DiBiase, Khoa Le, Larry Marshall, and Alan Hays, "High-power diode-pumped solid-state laser for Optical Space Communications," *SPIE Optical Space Communication II, 1522*: 169-180 (1991).
22. Koehler, Captain Charles A. *A Comparison Between the Ground-. Based Electro-Optical Deep Space Surveillance (GEODSS) System and a Proposed Visible Light Space-Based Sensor System for Deep Space Surveillance*. MS thesis, AFTT/GSO/ENS- ENP/86D-2. School of Engineering, Air Force Institute of Technology (AU). Wright Patterson AFB OH. December 1989 (AAI- 3692).
23. Kostishack, David F. "Small Satellite Sensors for Multi-Spectral Space . Surveillance," *Small Satellite and Applications*, edited by Brian J. Horais. Proc. SPIE 1495: 214-227.
24. Lange, Maj J. J. and Evans Lt Col H. E. *Electro-Optical Space Systems Technology*. Staff Notes for PHYS 621 Electro-Optical Space Systems Technology. School of Engineering, Air Force Institute of Technology (AU), Wright Patterson AFB OH, January 1989.

25. Levenstein, Harold "Laser Radar Based on Diode Lasers," *SPIE Laser Radar VI*, 1416: 30-43 (1991).
26. Malo, Major F., Senior Director 21st Aerospace and Control Squadron. Telephone Interview. Canadian NORAD Region, CFB North Bay, Ontario, Canada, 12 Aug 1992.
27. Marshalek, R. G. and Koepf, G. A. "Comparison of optical technologies for intersatellite links," *SPIE Optical Technologies for Communication Satellite Applications*, 616: 29-48 (1986).
28. Mayer, B.J. *Expected Energy Method for Electro-Optical SNR Calculations*. Contract F19628-80-C-0002. M.I.T. Lincoln Laboratory, Lexington, Mass., 2 Feb 1984 (AD A139 984).
29. McCoy, J., J. Daugherty, H. Hyman, M. Dunn, W. Caton, B. Neff, and S. Young "Portable Rapid Optical Beam Steering LADAR System," *SPIE Laser Radar VII*, 1633: 15-20 (1992).
30. Powell, Joel. "Satellite Tracking with GEODSS," *Spaceflight*, March 1985, pp. 129-130.
31. Randolph, Anne, "USAF Upgrades Deep Space Surveillance," *Aviation Week & Space Technology*, 28 February 1983, pp. 57-58.
32. Roddy, D. *Satellite Communications*. Prentice-Hill Inc, Englewood Cliffs, NJ, 1989.
33. Roggemann, Capt M. *Electro-Optical Space Systems Technology*. Staff Notes for PHYS 621 Electro-Optical Space Systems Technology. School of Engineering, Air Force Institute of Technology (AU), Wright Patterson AFB OH, January 1993.
34. Scifres, D.R., D.F. Welch, R.R. Craig, E. Zucker, J.S. Major, G.L. Harnagel, M. Sakamoto, J.M. Haden, J.G. Endriz and H. Kung "High Power, High Reliability Laser Diodes," *SPIE Laser Diode Technology and Applications IV* 1634: 192-197 (1992).
35. Skolnik, M. I. *Introduction to Radar Systems*. McGraw-Hill Book Company, New York, NY, 1980.
36. Skolnik, M.I., Ed. *Radar Handbook*. McGraw-Hill Book Company, New York, NY, 1970.
37. *Spectra Diode Labs*. 1993 Laser Diode Product Catalog, San Jose CA, no date (1993).

38. Stares, Paul B. *The Militarization of Space: U.S. Policy, 1945-1984*. Cornwell University Press, 1985.
39. USSPACECOM, Breifing slides, Nov 1992.
40. Van Dierendonck, A. J., S.S. Russell, E.R. Kopitzke and M. Birnbaum. "The GPS Navigation Message," Papers published in NAVIGATION, Volume I, Institute of Navigation, Washington, D.C., 1980.
41. Weber, Robert. *Visual Magnitude Flux Rate Density Standards for Sunlight Incident on Photoemissive Surfaces*. Contract F19628-73-C-0002. M.I.T. Lincoln Laboratory, Lexington , Mass., 6 May 1974 (AD 779 822).
42. Wolfe, William L., and Zissis George J. (editors) *The Infrared Handbook*. Office of Naval Research, Department of the Navy, Washington DC, 1978.
43. Yariv, A. *Introduction to Optical Electronics*. Holt, Rinehart, and Winston, New York, NY, 1976
44. Yoder, John and Youmans, Douglas "Laser radar wavelength selection and trade-offs," *SPIE Laser Radar III* 999: 72-83 (1988).

Vita •

Captain Bradley K. Fournier was born on 11 September 1962 in Calgary, Alberta (Canada). He joined the Canadian Armed Forces in 1980 and graduated from Royal Roads Military College in 1984 with a Bachelor of Science in Physics and Computer Science. He was trained as an Air Weapons Controller and employed in the Joint Surveillance System Regional Operations Control Center as a controller and software analyst until 1987. He was then posted to the System Integration Office in AFSPACCOM HQ in Colorado Springs where he was responsible for the testing and integration of all atmospheric sensors providing information to NORAD HQ. Following this assignment, he was selected to attend the Canadian Forces School of Aerospace Studies in 1987 for a one year course. After graduation he remained on staff for eight months to instruct until entering the School of Engineering, Air Force Institute of Technology, in May 1992.

Permanent Address: 444 Conway Street
Winnipeg, Manitoba
Canada
R3J 2M8

REPORT DOCUMENTATION PAGE			Form Approved ONR No. 0704-0198	
<small> This report is prepared for the Office of Naval Research, Department of the Navy, and is not to be distributed outside the Department of the Navy. It is not to be used for any other purpose without the written permission of the Office of Naval Research. It is not to be used for any other purpose without the written permission of the Office of Naval Research. It is not to be used for any other purpose without the written permission of the Office of Naval Research. </small>				
1. AGENCY USE ONLY (Leave blank)		2. REPORT DATE December 1993		3. REPORT TYPE AND DATES COVERED Master's Thesis
4. TITLE AND SUBTITLE DESIGN ANALYSIS OF A COMBINED OPTICAL/LADAR DEEP-SPACE SURVEILLANCE SATELLITE			5. FUNDING NUMBERS	
6. AUTHOR(S) Bradley K. Fournier, Captain, CAF				
7. PERFORMING ORGANIZATION NAME(S) AND ADDRESS(ES) Air Force Institute of Technology, WPAFB OH 45433-6583			8. PERFORMING ORGANIZATION REPORT NUMBER AFTT/GSO/ENG/93D-01	
9. SPONSORING/MONITORING AGENCY NAME(S) AND ADDRESS(ES) N/A			10. SPONSORING/MONITORING AGENCY REPORT NUMBER	
11. SUPPLEMENTARY NOTES				
12a. DISTRIBUTION/AVAILABILITY STATEMENT Approved for public release; distribution unlimited			12b. DISTRIBUTION CODE	
13. ABSTRACT (Maximum 200 words) <p>This research determines the performance requirements of a combined optical/LADAR space-based system in order to detect and track deep-space satellites from a near-earth orbit satellite. The research derives the necessary equations to compare both direct and heterodyne detection techniques. The selection of the candidate laser systems is based on current space-developed LADAR technology. The selection of the detector, detector size, and optic size are determined in order to maximize the signal-to-noise ratio. The analysis includes the effects of beam truncation, obscuration, pixel geometry and background radiance.</p> <p>The results indicate that the direct detection technique with a GaAlAs semiconductor laser and a charge-couple device detector provided the best signal-to-noise ratio for the range selected. In addition, the visible detection capability of the smallest entrance pupil system is compared with that of GEODSS. For the parameters chosen, the results indicate that this system should, on average, be able to detect objects of smaller size than GEODSS.</p>				
14. SUBJECT TERMS LADAR, Laser RADAR, Optical Detection, Satellite Detection, Optical RADAR			15. NUMBER OF PAGES 96	
			16. PRICE CODE	
17. SECURITY CLASSIFICATION OF REPORT Unclassified	18. SECURITY CLASSIFICATION OF THIS PAGE Unclassified	19. SECURITY CLASSIFICATION OF ABSTRACT Unclassified	20. LIMITATION OF ABSTRACT UL	